

1 **Examination of aerosol impacts on convective clouds and precipitation in two**
2 **metropolitan areas in East Asia; how varying depths of convective clouds between**
3 **the areas diversify those aerosol effects?**

4

5 Seoung Soo Lee^{1,2}, Jinho Choi³, Goun Kim⁴, Kyung-Ja Ha^{2,5,6}, Kyong-Hwan Seo³, Chang-
6 Hoon Jung⁷, Junshik Um³, Youtong Zheng⁸, Jianping Guo⁹, Sang-Keun Song¹⁰, Yun Gon
7 Lee¹¹, Nobuyuki Utsumi¹²

8

9 ¹Earth System Science Interdisciplinary Center, University of Maryland, Maryland

10 ²Research Center for Climate Sciences, Pusan National University, Busan, Republic of
11 Korea

12 ³Department of Atmospheric Sciences, Pusan National University, Busan, Republic of
13 Korea

14 ⁴Marine Disaster Research Center, Korea Institute of Ocean Science and Technology,
15 Pusan, Republic of Korea

16 ⁵Center for Climate Physics, Institute for Basic Science, Busan, Republic of Korea

17 ⁶BK21 School of Earth and Environmental Systems, Pusan National University, Busan,
18 Republic of Korea

19 ⁷Department of Health Management, Kyungin Women's University, Incheon, Republic of
20 Korea

21 ⁸The Program in Atmospheric and Oceanic Sciences, Princeton University, Princeton,
22 New Jersey, USA

23 ⁹State Key Laboratory of Severe Weather, Chinese Academy of Meteorological Sciences,
24 Beijing, China

25 ¹⁰Department of Earth and Marine Sciences, Jeju National University, Jeju, Republic of
26 Korea

27 ¹¹Department of Astronomy, Space Science and Geology, Chungnam National
28 University, Daejeon, Republic of Korea

29 ¹²Nagomori Institute of Actuators, Kyoto University of Advanced Science, Japan

30

31 Corresponding author: Seoung Soo Lee

32 Office: (303) 497-6615

33 Fax: (303) 497-5318

34 E-mail: cumulss@gmail.com, slee1247@umd.edu

35

36

37

38

39

40

41

42

43

44

45

46

47

48

49

50

51 Abstract

52

53 This study examines the role played by aerosols which act as cloud condensation nuclei
54 (CCN) in the development of clouds and precipitation in two metropolitan areas in East
55 Asia that have experienced substantial increases in aerosol concentrations over the last
56 decades. These two areas are the Seoul and Beijing areas and the examination has been
57 done by performing simulations using the Advanced Research Weather Research and
58 Forecasting model as a cloud-system resolving model. CCN are advected from the
59 continent to the Seoul area and this increases aerosol concentrations in the Seoul area.
60 These increased CCN concentrations induce the enhancement of condensation that in turn
61 induces the enhancement of deposition and precipitation amount in a system of less deep
62 convective clouds as compared to those in the Beijing area. In a system of deeper clouds
63 in the Beijing area, increasing CCN concentrations also enhance condensation but reduce
64 deposition. This leads to CCN-induced negligible changes in precipitation amount. Also,
65 in the system, there is a competition for convective energy among clouds with different
66 condensation and updrafts. This competition results in different responses to increasing
67 CCN concentrations among different types of precipitation, which are light, medium and
68 heavy precipitation in the Beijing area. CCN-induced changes in freezing play a negligible
69 role in CCN-precipitation interactions as compared to the role played by CCN-induced
70 changes in condensation and deposition in both of the areas.

71

72

73

74

75

76

77

78

79

80

81

1. Introduction

82
83
84 With increasing aerosol loading or concentrations, cloud-particle sizes can be changed. In
85 general, with increasing droplet sizes, the efficiency of collision and collection among
86 droplets increases. Increasing aerosol loading is known to make the droplet size smaller
87 and thus make the efficiency of collision and collection among droplets lower. This leads
88 to less droplets or cloud liquid forming raindrops and there is more cloud liquid present in
89 the air to be evaporated or frozen. Studies have shown that increases in cloud-liquid mass
90 due to increasing aerosol loading can enhance the freezing of cloud liquid and parcel
91 buoyancy, which lead to the invigoration of convection (Rosenfeld et al., 2008; Fan et al.,
92 2009). Via the invigoration of convection, precipitation can be enhanced. The dependence
93 of aerosol-induced invigoration of convection and precipitation enhancement on aerosol-
94 induced increases in condensational heating in the warm sector of a cloud system has been
95 shown (e.g., van den Heever et al., 2006; Fan et al., 2009; Lee et al., 2018). Increasing
96 cloud-liquid mass induces increasing evaporation, which intensifies gust fronts. This in
97 turn strengthens convective clouds and increases the amount of precipitation (Khain et al.,
98 2005; Tao et al., 2007; Storer et al., 2010; Tao et al., 2012; Lee et al., 2017; Lee et al.,
99 2018). It is notable that aerosol-induced precipitation enhancement is strongly sensitive to
100 cloud types that can be defined by cloud characteristics such as cloud depth (e.g., Tao et
101 al., 2007; Lee et al., 2008; Fan et al., 2009).

102 Since East Asia was industrialized, there have been substantial increases in aerosol
103 concentrations over the last decades in East Asia (e.g., Lee et al., 2013; Lu et al., 2011; Oh
104 et al., 2015; Dong et al., 2019). These increases are far greater than those in other regions
105 such as North America and Europe (e.g., Lu et al., 2011; Dong et al., 2019). While those
106 increasing aerosols affect clouds, precipitation and hydrologic circulations in the
107 continental East Asia, the increase in the advected aerosols from the continent to the
108 Korean Peninsula affect clouds, precipitation and hydrologic circulations in the Korean
109 Peninsula (Kar et al., 2009). This study aims to examine effects of the increasing aerosols,
110 which particularly act as cloud condensation nuclei (CCN), and their advection on clouds
111 and precipitation in East Asia. This study focuses on aerosols which act as CCN, but not
112 ice-nucleating particles (INPs), to examine those effects, based on the fact that CCN

113 account for most of aerosol mass that affects clouds and precipitation, and CCN, but not
114 INPs, are associated with above-described aerosol-induced invigoration of convection and
115 intensification of gust fronts. Note that these aerosol-induced invigoration and
116 intensification are two well-established major theories of aerosol-cloud interactions. As a
117 first step to the examination, this study focuses on two metropolitan areas in East Asia
118 which are the Beijing and Seoul areas. The population of each of the Beijing and Seoul
119 areas is ~ 20 millions. Associated with this, these areas have lots of aerosol sources (e.g.,
120 traffic) and have made a substantial contribution to the increases in aerosol concentrations
121 in East Asia. Hence, we believe that these two cities can represent overall situations related
122 to increasing aerosol concentrations in East Asia.

123 As mentioned above, aerosol-cloud interactions (and their impacts on precipitation) are
124 strongly dependent on cloud types and thus to gain a more general understanding of those
125 interactions, we select cases from the Beijing and Seoul areas with different cloud types.
126 A selected case from the Beijing area involves deep convective clouds that reach the
127 tropopause, while a selected case from the Seoul area involves comparatively shallow (or
128 less deep) convective clouds. Via comparisons between these two cases, we aim to identify
129 mechanisms that control varying aerosol-cloud interactions with cloud types.

130 To examine impacts of aerosols, which act as CCN, on clouds and precipitation in the
131 cases, numerical simulations are performed, as a way of fulfilling above-described aim.
132 These simulations use a cloud-system resolving model (CSRМ) that has reasonably high
133 resolutions to resolve cloud-scale processes that are related to cloud microphysics and
134 dynamics. Hence, these simulations are able to find process-level mechanisms in
135 association with cloud-scale processes.

136

137 **2. Case description**

138

139 In the Seoul area, South Korea, there is an observed mesoscale convective system (MCS)
140 for a period from 03:00 LST (local solar time) to 18:00 LST December 24th 2017. During
141 this period, there is a recorded moderate amount of precipitation and its maximum
142 precipitation rate reaches ~ 13 mm hr⁻¹. Here, precipitation in the Seoul area is measured
143 by rain gauges in automatic weather stations (AWSs) (King, 2009). The measurement is

144 performed hourly with a spatial resolution that ranges from ~1 km to ~10 km. The Seoul
145 area is marked by an inner rectangle in Figure 1a and dots in the rectangle in Figure 1a
146 mark the selected locations of rain gauges. At 21:00 LST December 23rd 2017, synoptic-
147 scale features develop in favor of the formation and development of the selected MCS and
148 associated moderate rainfall. These features involve the southwesterly low-level jets that
149 transport warm and moist air to the Korean Peninsula. The southwesterly low-level jet
150 plays an important role in the formation and development of rainfall events in the Korean
151 Peninsula by fetching warm and moist air (Hwang and Lee 1993; Lee et al. 1998; Seo et
152 al. 2013; Oh et al. 2018).

153 There was another observed MCS case in the Beijing area, China for a period from
154 14:00 LST on July 27th to 00:00 LST July 28th 2015. There is a substantial recorded amount
155 of precipitation for this period and its maximum precipitation rate reaches ~ 45 mm hr⁻¹.
156 Here, similar to the situation in the Seoul area, precipitation in the Beijing area is measured
157 by rain gauges in AWSs hourly with a spatial resolution that ranges from ~1 km to ~10 km.
158 The Beijing area is marked by an inner rectangle in Figure 1b and dots in the rectangle in
159 Figure 1b mark the selected locations of rain gauges. At 09:00 LST July 27th 2015,
160 synoptic-scale features develop in favor of the formation and development of the selected
161 MCS. These features involve the southerly low-level jet that develops heavy rainfall events
162 in the Beijing area by transporting warm and moist air to the area. Synoptic features which
163 are described here are based on reanalysis data that are produced by the Met Office Unified
164 Model (Brown et al., 2012) every 6 hours with a $0.11^\circ \times 0.11^\circ$ resolution.

165

166 **3. CSRM and simulations**

167

168 **3.1 CSRM**

169

170 The Advanced Research Weather Research and Forecasting (ARW) model (version 3.3.1)
171 is used as a CSRM. The ARW model is a compressible model with a nonhydrostatic status.
172 A 5th-order monotonic advection scheme is used to advect microphysical variables (Wang
173 et al., 2009). The Rapid Radiation Transfer Model (RRTMG; Mlawer et al., 1997; Fouquart
174 and Bonnel, 1980) is adopted to parameterize shortwave and longwave radiation in

175 simulations. A microphysics scheme that is used in this study calculates the effective sizes
176 of hydrometeors that are fed into the RRTMG, and the RRTMG simulates how these
177 effective sizes affect radiation.

178 The CSRM adopts a bin scheme as a way of parameterizing microphysics. The
179 Hebrew University Cloud Model (HUCM) detailed in Khain et al. (2011) is the bin scheme.
180 A set of kinetic equations is solved by the bin scheme to represent a size distribution
181 function for each of seven classes of hydrometeors and aerosols acting as CCN. Hence,
182 there are seven size distribution functions for hydrometeors. The seven classes of
183 hydrometeors are water drops, three types of ice crystals, which are plates, columns and
184 dendrites, snow aggregates, graupel and hail. Drops whose radius is smaller (larger) than
185 $40\ \mu\text{m}$ are categorized to be droplets (raindrops). There are 33 bins for each size
186 distribution in a way that the mass of a particle m_j in the j bin is to be $m_j = 2m_{j-1}$.

187 A cloud-droplet nucleation parameterization based on Köhler theory represents cloud-
188 droplet nucleation. Arbitrary aerosol mixing states and aerosol size distributions can be fed
189 to this parameterization. To represent heterogeneous ice-crystal nucleation,
190 parameterizations by Lohmann and Diehl (2006) and Möhler et al. (2006) are used. In these
191 parameterizations, contact, immersion, condensation-freezing, and deposition nucleation
192 paths are all considered by taking into account the size distribution of INPs, temperature
193 and supersaturation. Homogeneous droplet freezing is
194 considered following the theory developed by Koop et al. (2000).

195

196 **3.2 Control runs**

197

198 For a three-dimensional CSRM simulation of the observed case of convective clouds in the
199 Seoul (Beijing) area, i.e., the control-s (control-b) run, a domain just over the Seoul
200 (Beijing) area, which is shown in Figure 1a (1b), is used. This domain adopts a 300-m
201 resolution. The control-s run is for a period from 03:00 LST to 18:00 LST December 24th
202 2017, while the control-b run is for a period from 14:00 LST on July 27th to 00:00 LST
203 July 28th 2015. The length of the domain is 170 (140) km in the east-west (north-south)
204 direction for the control-s run, and 280 (240) km for the control-b run. There are 100
205 vertical layers and these layers employ a sigma coordinate that follows the terrain. The top

206 pressure of the model is 50 hPa for both of the control-s and control-b runs. On average,
207 the vertical resolution is ~200 m.

208 Reanalysis data, which are produced by the Met Office Unified Model (Brown et al.,
209 2012), represent the synoptic-scale features, provide initial and boundary conditions of
210 variables such as wind, potential temperature, and specific humidity for the simulations.
211 The simulations adopt an open lateral boundary condition. The Noah land surface model
212 (LSM; Chen and Dudhia, 2001) calculates surface heat fluxes.

213 The current version of the ARW model is not able to consider the spatiotemporal
214 variation of aerosol properties. In order to take into account the spatiotemporal variation of
215 aerosol properties, which is typical in metropolitan areas, such as composition and number
216 concentration, an aerosol preprocessor, which is able to consider the variability of aerosol
217 properties, is developed and used in the simulations. This aerosol preprocessor interpolates
218 or extrapolates background aerosol properties in observation data such as aerosol mass
219 (e.g., PM_{2.5} and PM₁₀) into grid points and time steps in the model. In this study, the inverse
220 distance weighting method is used for the extrapolation and interpolation of observation
221 data including aerosol mass into grid points and time steps in the model. PM stands for
222 particulate matter. The mass of aerosols with diameter smaller than 2.5 (10.0) μm per unit
223 volume of the air is PM_{2.5} (PM₁₀).

224 There are surface observation sites, which measure aerosol properties, in the domains
225 and these sites are classified into two types; the selected locations of these sites are marked
226 by dots in the inner rectangles in Figure 1. The distance between the observation sites
227 ranges from ~1 km to ~10 km and the time interval between observations is ~10 minutes.
228 More than 90% of the sites belong to the first type of the sites. These first-type sites are
229 managed by the government in South Korea or China, and measure PM_{2.5} or PM₁₀ but not
230 other aerosol properties such as aerosol composition and size distributions. Less than 10%
231 of the sites belong to the second type of the sites. These second-type sites are a part of
232 aerosol robotic network (AERONET; Holben et al., 2001) and measure aerosol
233 composition and size distributions. The production of aerosol data in these second-type or
234 AERONET sites is viable only in the presence of the sun. The first-type sites observe PM_{2.5}
235 or PM₁₀ using the beta-ray attenuation method (Eun et al., 2016; Ha et al., 2019) and hence,
236 produce PM_{2.5} or PM₁₀ data whether the sun is present or not. PM_{2.5}/PM₁₀ data from the

237 first-type sites are used to represent the spatiotemporal variability of aerosols over the
238 domains and the simulation periods. To represent aerosol composition and size
239 distributions, data from the AERONET sites are employed.

240 The AERONET data are averaged over the AERONET sites at 02:00 LST December
241 24th 2017 (13:00 LST July 27th 2015), which is 1 hour before the observed MCS forms, for
242 the Seoul (Beijing) case. Based on the average data, it is assumed that aerosol particles are
243 internally mixed with 70 (80) % ammonium sulfate and 30 (20) % organic compound for
244 the Seoul (Beijing) case. This mixture is assumed to represent aerosol chemical
245 composition in the whole domain and during the entire simulation period. Since ammonium
246 sulfate and organic compound are representative components of CCN, it is assumed that
247 $PM_{2.5}$ and PM_{10} , which are from the first-type sites, represent the mass of aerosols that act
248 as CCN for the Seoul and Beijing areas, respectively. Aerosols reflect, scatter and absorb
249 shortwave and longwave radiation before they are activated. This type of aerosol-radiation
250 interactions is not taken into account in this study. This is mainly based on the fact that in
251 the mixture, there is insignificant amount of radiation absorbers; black carbon is a
252 representative radiation absorber. The average AERONET data indicate that the size
253 distribution of background aerosols acting as CCN follows the bi-modal log-normal
254 distribution for both of the Seoul and Beijing cases. Based on the average AERONET data,
255 it is assumed that for the whole domain and simulation period, the size distribution of
256 background aerosols acting as CCN follows a shape of distribution with specific size
257 distribution parameters (i.e., modal radius and standard deviation of each of accumulation
258 and coarse modes, and the partition of aerosol number among those modes) for each of the
259 cases. Modal radius of the shape of distribution is 0.110 (0.085) and 1.413 (1.523) μm ,
260 while standard deviation of the shape of distribution is 1.54 (1.63) and 1.75 (1.73) for
261 accumulation and coarse modes, respectively, in the Seoul (Beijing) case. The partition of
262 aerosol number, which is normalized by the total aerosol number of the size distribution,
263 is 0.999 and 0.001 for accumulation and coarse modes, respectively, in both of the cases.
264 By using $PM_{2.5}$ or PM_{10} , which is not only from the first-type sites but also interpolated
265 and extrapolated to grid points immediately above the surface and time steps, and based on
266 the assumption of aerosol composition and size distribution above, which is in turn based
267 on data from the AERONET sites, the background number concentrations of aerosols

268 acting as CCN are obtained for the simulation for each of the cases. There is no variation
269 with height in background concentrations of aerosols acting as CCN from immediately
270 above the surface to the top of the planetary boundary layer (PBL). However, it is assumed
271 that they decrease exponentially with height from the PBL top upward. With this
272 exponential decrease, when the altitude reaches the tropopause, background concentrations
273 of aerosols acting as CCN reduce by a factor of ~ 10 as compared to those at the PBL top.
274 The size distribution and composition of aerosols acting as CCN do not vary with height.
275 Once background aerosol properties (i.e., aerosol number concentrations, size distribution
276 and composition) are put into each grid point and time step, those properties at each grid
277 point and time step do not change during the course of the simulations.

278 For the control-s and control-b runs, aerosol properties of INPs are not different from
279 those of CCN except for the fact that the concentration of background aerosols acting as
280 CCN is 100 times higher than the concentration of background aerosols acting as INPs at
281 each time step and grid point, following a general difference between CCN and INPs in
282 terms of their concentrations (Pruppacher and Klett, 1978).

283 Once clouds form and background aerosols start to be in clouds, those aerosols are
284 not background aerosols anymore and the size distribution and concentrations of those
285 aerosols begin to evolve through aerosol sinks and sources that include advection and
286 aerosol activation (Fan et al., 2009). For example, once aerosols are activated, they are
287 removed from the corresponding bins of the aerosol spectra. In clouds, after aerosol
288 activation, aerosol mass starts to be inside hydrometeors and via collision-collection, it
289 transfers to different types and sizes of hydrometeors. In the end, aerosol mass disappears
290 in the atmosphere when hydrometeors with aerosol mass touches the surface. In non-cloudy
291 areas, aerosol size and spatial distributions are designed to be identical to the size and
292 spatial distributions of background aerosols, respectively. In other words, for this study,
293 we use “the aerosol recovery method”. In this method, at any grid points, immediately after
294 clouds disappear entirely, aerosol size distributions and number concentrations recover to
295 background properties that background aerosols at those points have before those points
296 are included in clouds. In this way, we can keep concentrations of background aerosols
297 outside clouds in the simulations at observed counterparts. This enables spatiotemporal
298 distributions of background aerosols in the simulations to mimic those distributions that

299 are observed and particularly associated with observed aerosol advection in reality. In the
300 aerosol recovery method, there is no time interval between the cloud disappearance and the
301 aerosol recovery. Here, when the sum of mass of all types of hydrometeors (i.e., water
302 drops, ice crystals, snow aggregates, graupel and hail) is not zero at a grid point, that grid
303 point is considered to be in clouds. When this sum becomes zero, clouds are considered to
304 disappear. Many studies using CSRM have employed this aerosol recovery method. They
305 have proven that with the recovery method, reasonable simulations of overall cloud and
306 precipitation properties are accomplished (e.g., Morrison and Grabowski, 2011; Lebo and
307 Morrison, 2014; Lee et al., 2016; Lee et al., 2018).

308

309

3.3 Additional runs

310

311 We repeat the control-s run by getting rid of aerosol-advection induced increases in
312 concentrations of aerosols acting as CCN as a way of investigating how the aerosol
313 advection affects the cloud system in the Seoul area. This repeated run is named the low-
314 aerosol-s run. An aerosol layer, which is advected from East Asia or from the west of the
315 Seoul area to it, increases aerosol concentrations in the Seoul area. There are stations in
316 islands in the Yellow Sea that monitor the aerosol advection (Eun et al., 2016; Ha et al.,
317 2019). To monitor and identify the aerosol advection, $PM_{2.5}$ which is measured by a station
318 in Baekryongdo island in Yellow Sea are compared to those which are measured in stations
319 in and around the Seoul area. In Figure 1a, a dot outside the inner rectangle marks the
320 island. The time evolution of $PM_{2.5}$ measured by the station on the island and the average
321 $PM_{2.5}$ over stations in the Seoul area, between 07:00 LST on December 22nd and 21:00 LST
322 on December 24th in 2017 when there is the strong advection of aerosols from East Asia to
323 the Seoul area, is shown in Figure 2. At 09:00 LST on December 22nd, the advection of
324 aerosols from East Asia enables aerosol mass to start going up and attain its peak around
325 05:00 LST on December 23rd on the island. Following this, aerosol mass starts to increase
326 in the Seoul area around 01:00 LST on December 23rd, and the mass attains its peak at
327 15:00 LST on December 23rd in the Seoul area. This is because aerosols, which are
328 advected from East Asia, move through the island to reach the Seoul area.

329 In the low-aerosol-s run, as a way of getting rid of aerosol-advection induced increases
330 in concentrations of aerosols acting as CCN, it is assumed that $PM_{2.5}$, which is assumed to
331 represent the mass of aerosols acting as CCN, and the associated background concentration
332 of aerosols acting as CCN after 01:00 LST on December 23rd do not evolve with the aerosol
333 advection in the Seoul area. Hence, the background concentration of aerosols acting as
334 CCN is assumed to have that at 01:00 LST on December 23rd at each time step and grid
335 point at the beginning of the simulation period. However, to isolate CCN effects on clouds,
336 background aerosol concentration acting as INPs at each time step and grid point in the
337 low-aerosol-s run is not different from that in the control-s run during the simulation period.
338 In the observed PM data for the Seoul area, there is reduction in PM by a factor of ~ 10 on
339 average over a period between $\sim 07:00$ and $\sim 14:00$ LST on December 24th, since
340 precipitation scavenges aerosols (Figure 2). To emulate this scavenging and reflect it in
341 background aerosols acting as CCN for the low-aerosol-s run, $PM_{2.5}$ and corresponding
342 background concentrations of aerosols acting as CCN at each grid point is gradually
343 reduced for the period between 07:00 and 14:00 LST on December 24th. This reduction is
344 done in a way that background concentrations of aerosols acting as CCN at each grid point
345 at 14:00 LST on December 24th is 10 times lower than that at 07:00 LST on December 24th
346 in the low-aerosol-s run. Then, $PM_{2.5}$ and corresponding background concentrations of
347 aerosols acting as CCN at each grid point at 14:00 LST on December 24th maintains until
348 the end of the simulation period. This results in the evolution of the average $PM_{2.5}$ over the
349 Seoul area in the low-aerosol-s run as shown in Figure 2. Here, the concentration of
350 background aerosols acting as CCN, which is averaged over the whole domain and
351 simulation period, in the control-s run is 3.1 times higher than that in the low-aerosol-s run.
352 Via comparisons between the runs, how the increasing concentration of background
353 aerosols acting as CCN due to the aerosol advection has an impact on clouds can be
354 examined. The concentration of background aerosols acting as CCN is different among
355 grid points and time steps in the control-s run. Hence, the ratio of the concentration of
356 background aerosols acting as CCN between the runs is different among grid points and
357 time steps.

358 For the Beijing case, to examine how aerosols acting as CCN affect clouds and
359 precipitation, we repeat the control-b run with simply reduced concentrations of

360 background aerosols acting as CCN at each time step and grid point by a factor of 3.1. This
361 repeated run is named the low-aerosol-b run. The 3.1-fold increase in aerosol
362 concentrations from the low-aerosol-b run to the control-b is based on the 3.1-fold increase
363 in the average concentration of background aerosols acting as CCN from the low-aerosol-
364 s run to the control-s run. However, as in the control-s and low-aerosol-s runs, to isolate
365 CCN effects on clouds, background aerosol concentration acting as INPs at each time step
366 and grid point in the low-aerosol-b run is identical to that in the control-b run during the
367 simulation period. Hence, on average, a pair of the control-s and low-aerosol-s runs has the
368 same perturbation of aerosols acting as CCN as in a pair of the control-b and low-aerosol-
369 b runs. Here, we define aerosol perturbation as a relative increase in aerosol concentration
370 when compared to that before the increase occurs. The brief summary of all simulations in
371 this study is given in Table 1.

372

373 **4. Results**

374

375 **4.1 Cumulative precipitation**

376

377 We compare the observed precipitation to the simulated counterpart in the control-s run for
378 the Seoul case and in the control-b run for the Beijing case. For this comparison, the
379 observed and simulated precipitation rates at the surface are averaged over the domain for
380 each of the Seoul and Beijing cases (Figures 3a and 3b). Here, the simulated precipitation
381 rates are smoothed over 1 hour. The comparison shows that the evolution of the simulated
382 precipitation rate does not deviate from the observed counterpart significantly (Figures 3a
383 and 3b).

384 In the Seoul case, overall, the precipitation rate is higher in the control-s run than in
385 the low-aerosol-s run. As a result of this, the domain-averaged cumulative precipitation
386 amount at the last time step is 14.1 mm and 12.0 mm in the control-s run and the low-
387 aerosol-s run, respectively. The control-s run shows ~20 % higher cumulative precipitation
388 amount. In the Beijing case, the evolution of the mean precipitation rate in the control-b
389 run is not significantly different from that in the low-aerosol-b run. Due to this, the control-
390 b run shows only ~2 % higher cumulative precipitation amount, despite the fact that the

391 concentrations of background aerosols acting as CCN are ~ 3 times higher in the control-b
392 run than in the low-aerosol-b run. Note that in the Seoul case, the time- and domain-
393 averaged concentration of background aerosols acting as CCN is also ~ 3 times higher in
394 the control-s run than in the low-aerosol-s run. Despite this, the difference in the cumulative
395 precipitation amount between the runs with different concentrations of background
396 aerosols acting as CCN is greater in the Seoul case than in the Beijing case.

397

398 **4.2 Precipitation, and associated latent-heat and dynamic processes**

399

400 Figures 4a and 4b show the cumulative frequency distributions of precipitation rates at the
401 last time step in the simulations for the Seoul and Beijing cases, respectively. In each of
402 those figures, the observed frequency distribution is shown and compared to the simulated
403 distribution. The observed distribution is obtained by interpolating and extrapolating the
404 observed precipitation rates to grid points and time steps in each of the control-s and
405 control-b runs. The observed maximum precipitation rates are 13.0 and 44.5 mm hr⁻¹ for
406 the Seoul and Beijing cases, respectively, and these maximum rates are similar to those in
407 the control-s and control-b runs, respectively. Overall, the observed and simulated
408 frequency distributions are in good agreement for each of the cases. This enables us to
409 assume that results in the control-s (control-b) run are benchmark results to which results
410 in the low-aerosol-s (low-aerosol-b) run can be compared to identify how aerosols acting
411 as CCN have an impact on clouds and precipitation for the Seoul (Beijing) case. Here, it is
412 notable that for the Beijing case, while differences in the cumulative precipitation amount
413 between the control-b and low-aerosol-b runs are not significant, features in the frequency
414 distribution of precipitation rates between those runs are substantially different (Figure 4b).

415

416 **1) Seoul case**

417

418 **a. Precipitation Frequency distributions**

419

420 Regarding precipitation whose rates are higher than ~ 2 mm hr⁻¹, the cumulative
421 precipitation frequency at the last time step is higher in the control-s run as compared to

422 that in the low-aerosol-s run (Figure 4a). In particular, for the precipitation rate of 11.4 mm
423 h^{-1} , there is an increase in the cumulative frequency by a factor of as much as ~ 10 in the
424 control-s run. When it comes to precipitation rates above 11.5 mm hr^{-1} , precipitation is
425 present in the control-s run and precipitation is absent in the low-aerosol-s run. Regarding
426 precipitation whose rates are lower than $\sim 2 \text{ mm hr}^{-1}$, differences in the cumulative
427 frequency between the runs are insignificant. Hence, we see that there are significant
428 increases in the frequency of relatively heavy precipitation whose rates are above $\sim 2 \text{ mm}$
429 hr^{-1} in the control-s run when compared to that in the low-aerosol-s run. At the last time
430 step, this results in a larger amount of cumulative precipitation in the control-s run than in
431 the low-aerosol-s run.

432 The time evolution of the cumulative precipitation frequency is shown in Figure 5. At
433 06:00 LST December 24th 2017, which corresponds to the initial stage of the precipitation
434 development, the maximum precipitation rate reaches $\sim 3 \text{ mm hr}^{-1}$ and there is the greater
435 frequency over most of precipitation rates in the control-s run than in the low-aerosol-s run
436 (Figure 5a). With the time progress from 06:00 LST to 10:00 LST, the maximum
437 precipitation rate increases to reach 12 mm hr^{-1} and the cumulative frequency is higher over
438 precipitation whose rates are higher than $\sim 3 \text{ mm hr}^{-1}$ in the control-s run, while for
439 precipitation whose rates are lower than $\sim 3 \text{ mm hr}^{-1}$, differences in the cumulative
440 frequency between the runs are negligible (Figures 5a and 5b). When time reaches 12:00
441 LST, which is around time when the peak in the evolution of the area-averaged
442 precipitation rates occurs and thus the system is at its mature stage, the maximum
443 precipitation rate increases up to $\sim 13 \text{ mm hr}^{-1}$ (Figures 3a and 5c). The basic patterns of
444 differences in the cumulative precipitation frequency between the runs with the maximum
445 precipitation rate around 13 mm hr^{-1} , which are established at 12:00 LST, maintain until
446 the end of the simulation period (Figures 4a and 5c).

447

448 **b. Condensation, deposition, updrafts and associated variables**

449

450 Note that the source of precipitation is precipitable hydrometeors which are raindrops,
451 snow, graupel and hail particles. Droplets and ice crystals are the source of those
452 precipitable hydrometeors mostly via collision and coalescence processes. Droplets and ice

453 crystals gain their mass mostly via condensation and deposition. Based on this, to explain
454 the greater cumulative precipitation amount in the control-s run than in the low-aerosol-s
455 run, the evolutions of differences in condensation, deposition and associated updrafts
456 between the runs are analyzed. The vertical profiles of differences in the area-averaged
457 condensation, deposition and freezing rates, updraft mass fluxes and the associated mass
458 density of each class of hydrometeors between the runs at 03:20, 03:40, 06:00 and 12:00
459 LST are shown in Figure 6. In Figure 6, differences in freezing rates are added for a more
460 comprehensive understanding of processes that are related to differences in cumulative
461 precipitation amount between the runs. Freezing includes riming processes between liquid
462 and solid hydrometeors and these riming processes act as a source of precipitable
463 hydrometeors. Cloud fractions are 0.32 (0.30), 0.85 (0.82), 0.93 (0.92) and 1.00 (1.00) in
464 the control-s (low-aerosol-s) run at 03:20, 03:40, 06:00 and 12:00 LST, respectively. We
465 see that cloud fraction varies 0~6% between the runs. Note that in all of figures, which
466 display snow and hail mass density and include Figure 6, snow mass density includes ice-
467 crystal mass density, while hail mass density includes graupel mass density for the sake of
468 the display brevity. In Figure 6, horizontal black lines represent the altitudes of freezing
469 and melting.

470 Condensation rates in the control-s run start to be larger than that in the low-aerosol-
471 s run at 03:20 LST (Figure 6a). Higher aerosol or CCN concentrations induce more
472 nucleation of droplets, higher cloud droplet number concentration (CDNC) and associated
473 greater integrated surface of droplets in the control-s run. CDNC, which is averaged over
474 grid points and time steps with non-zero CDNC, is 1050 and 352 cm^{-3} in the control-s and
475 low-aerosol-s runs, respectively. Hence, more droplet surface is provided for water vapor
476 to condense onto in the control-s run. This leads to more condensation in the control-s run.
477 This establishes stronger feedbacks between updrafts and condensation, leading to greater
478 droplet (or cloud-liquid) mass at 03:20 LST in the control-s run (Figure 6a). Then, these
479 stronger feedbacks, which involve stronger updrafts particularly above 2 km in altitude,
480 subsequently induce greater deposition and snow mass as time progresses from 03:20 LST
481 to 03:40 LST, while more condensation and greater droplet mass maintain in the control-s
482 run with the time progress to 03:40 LST (Figure 6b). These stronger updrafts enable clouds
483 to grow higher in the control-s run. This eventually leads to a situation where the maximum

484 cloud depth is ~ 7 km in the control-s run and this depth is ~ 5 % deeper than that in the low-
485 aerosol-s run for the whole simulation period.

486 Through aerosol-induced stronger feedbacks between condensation, deposition and
487 updrafts in the control-s run, while more condensation and more overall deposition
488 maintain in the control-s run, differences in condensation and deposition between the
489 control-s and low-aerosol-s runs increase as time progresses from 03:40 LST to 06:00 LST
490 (Figures 6b and 6c). Associated with this, the greater mass of raindrops and hail particles
491 appears up, while the greater mass of droplets and snow in the control-s run than in the
492 low-aerosol-s run maintains with the time progress from 03:40 LST to 06:00 LST (Figure
493 6c). At 06:00 LST, there is more freezing starting to occur in the control-s run than in the
494 low-aerosol-s run. However, differences in freezing are \sim one and \sim two orders of magnitude
495 smaller than those in deposition and condensation, respectively. After 06:00 LST until time
496 reaches 12:00 LST when the overall differences in the cumulative precipitation frequency
497 between the runs are established, differences in freezing become ~ 3 times smaller than
498 those in deposition and \sim one order of magnitude smaller than those in condensation
499 (Figures 6c and 6d). The greater mass of hydrometeors in the control-s run also continues
500 after 06:00 LST until time reaches 12:00 LST (Figures 6c and 6d). At 12:00 LST,
501 condensation, deposition and freezing rates are still higher in the control-s run. Here, we
502 see that CCN-induced more cumulative precipitation amount and associated differences in
503 the precipitation frequency distribution between the control-s and low-aerosol-s runs are
504 primarily associated with CCN-induced more condensation, which induce CCN-induced
505 more deposition and higher mass density of hydrometeors as sources of precipitation, but
506 weakly connected to CCN-induced changes in freezing. This is supported by the fact that
507 the time- and domain-averaged differences in freezing rate are \sim one to \sim two order of
508 magnitude smaller than those in condensation and deposition rates.

509

510 **c. Condensation frequency distributions and horizontal distributions of** 511 **condensation and precipitation**

512

513 Based on the importance of condensation for CCN-induced changes in precipitation, the
514 horizontal distribution of the column-averaged condensation rates over the domain and the

515 cumulative frequency distribution of the column-averaged condensation rates at each time
516 step is obtained. To better visualize the role of condensation in precipitation, the horizontal
517 distribution of the column-averaged condensation rates is superimposed on that of
518 precipitation rates (Figure 7). At 03:40 LST, condensation mainly occurs around the
519 northern part of the domain as marked by a yellow rectangle. The synoptic wind condition
520 in the marked area favors the collision between northward and southward wind and the
521 associated convergence around the surface (Figures 7a and 7b). This convergence induces
522 updrafts and condensation in the marked area. In the marked area, more aerosols acting as
523 CCN induce more and more extensive condensation, which leads to the higher domain-
524 averaged condensation rates in the control-s run than in the low-aerosol-s run (Figures 6b,
525 7a and 7b). More droplets are formed on more aerosols acting as CCN and more droplets
526 provide more surface areas where condensation occurs and this enables more and more
527 extensive condensation in the control-s run than in the low-aerosol-s run (Figures 6b, 7a
528 and 7b).

529 At 06:20 LST, a precipitating system is advected into the domain via the western
530 boundary, and as seen in Figures 7c and 7d for 08:40 LST, as time progresses to 08:40 LST,
531 the advected precipitating system is further advected to the east and extended mostly over
532 areas in the northern part of the domain where condensation mainly occurs. This confirms
533 that condensation is the main source of cloud mass and precipitation. In the eastern part of
534 the domain, there are mountains and in particular, higher mountains are on the northeastern
535 part of the domain than in the other parts of the domain. These higher mountains induce
536 forced convection and associated condensation more effectively in the northeastern part
537 than in the other parts. This is in favor of the precipitating system that extends further to
538 the east in the northern part of the domain. Due to more aerosols acting as CCN,
539 condensation, which is induced by forced convection over mountains, is more and more
540 extensive in the control-s run (Figures 7c and 7d). In association with this, there is more
541 extension of the precipitating system in the control-s run than in the low-aerosol-s run. This
542 enables the system in the control-s run to reach the eastern boundary at 08:40 LST, which
543 is earlier than in the low-aerosol-s run (Figures 7c and 7d). The system in the low-aerosol-
544 s run reaches the eastern boundary at 09:00 LST. Here, we see that although aerosols acting
545 as CCN do not change overall locations of the precipitation system, they affect how fast

546 the system extends to the east by affecting the amount of condensation which is produced
547 by forced convection. Associated with this, as seen in Figure 8, the control-s run has the
548 much higher cumulative condensation frequency than the low-aerosol-s run over all of
549 condensation rates during the period between 07:20 and 09:00 LST. Contributed by this,
550 the higher precipitation frequency over most of precipitation rates occurs in the control-s
551 run during and after the period (Supplementary Figures 1a and 1b and Figures 5b and 5c).

552 At 10:00 LST, in the southern part of the domain, there is a precipitating area forming
553 as marked by a yellow rectangle (Figures 7e and 7f). The precipitation area in the southern
554 part of the domain extends and merges into the advecting main precipitating system in the
555 northern part of the domain. The merge leads to precipitation that occupies most of the
556 domain at 12:00 LST (Figures 7g and 7h). After 10:00 LST, associated with this merge,
557 the maximum precipitation rate increases to 13 mm hr^{-1} at 12:00 LST (Figures 5c). After
558 13:00 LST, the precipitation enters its dissipating stage and its area reduces and nearly
559 disappears. Even after the merge, CCN-induced more condensation maintains and this in
560 turn contributes to a situation where the control-s run has the greater precipitation
561 frequency over most of precipitation rates than in the low-aerosol-s run until the
562 simulations progress to their last time step (Figures 4a, 5c and 6d).

563

564 **2) Beijing case**

565

566 Stronger convection and deeper clouds develop in the Beijing case than in the Seoul case.
567 The maximum cloud depth is ~ 7 and ~ 12 km in the control-s and control-b runs,
568 respectively. In the Seoul case, clouds do not reach the tropopause, while they reach the
569 tropopause in the Beijing case. Deeper clouds in the Beijing case produce the maximum
570 precipitation rate of $\sim 45 \text{ mm hr}^{-1}$ in the control-b run. However, less deep clouds in the
571 Seoul case produce the maximum precipitation rate of $\sim 13 \text{ mm hr}^{-1}$ in the control-s run
572 (Figure 4).

573

574 **a. Precipitation frequency distributions**

575

576 When it comes to precipitation whose rates are higher than $\sim 12 \text{ mm hr}^{-1}$, the control-b run
577 has the higher cumulative precipitation frequency at the last time step than the low-aerosol-
578 b run (Figure 4b). Particularly, for the precipitation rates of 28.1 and 30.0 mm hr^{-1} , the
579 cumulative frequency increases by a factor of as much as ~ 10 . Moreover, regarding
580 precipitation rates higher than $\sim 33 \text{ mm hr}^{-1}$, precipitation is present in the control-b run,
581 however, precipitation is absent in the low-aerosol-b run. Hence, we see that the frequency
582 of comparatively heavy precipitation whose rates are higher than $\sim 12 \text{ mm hr}^{-1}$ rises
583 significantly in the control-b run as compared to that in the low-aerosol-b run. Below ~ 2
584 mm hr^{-1} , there is also the greater precipitation frequency in the control-b run than in the
585 low-aerosol-b run. Unlike the situation for precipitation rates above $\sim 12 \text{ mm hr}^{-1}$ and below
586 $\sim 2 \text{ mm hr}^{-1}$, for precipitation rates from $\sim 2 \text{ mm hr}^{-1}$ to $\sim 12 \text{ mm hr}^{-1}$, the control-aerosol-b
587 run has the lower precipitation frequency than in the low-aerosol-b run. Here, we see that
588 the higher precipitation frequency above $\sim 12 \text{ mm hr}^{-1}$ and below $\sim 2 \text{ mm hr}^{-1}$ balances out
589 the lower precipitation frequency between ~ 2 and $\sim 12 \text{ mm hr}^{-1}$ in the control-b run. This
590 results in the similar cumulative precipitation amount between the runs.

591 Figure 9 shows the time evolution of the cumulative precipitation frequency. When
592 precipitation starts around 16:00 LST, the higher precipitation frequency occurs over most
593 of precipitation rates in the low-aerosol-run-b run than in the control-b run (Figure 9a). At
594 16:00 LST, the maximum precipitation rate is lower than 1.0 mm hr^{-1} for both of the runs.
595 As time progresses to 17:00 LST, the maximum precipitation rate increases to $\sim 17 \text{ mm hr}^{-1}$
596 and the higher (lower) cumulative precipitation frequency over precipitation rates higher
597 than $\sim 12 \text{ mm hr}^{-1}$ (between ~ 2 and $\sim 12 \text{ mm hr}^{-1}$) in the control-b run than in the low-
598 aerosol-b run, which is described above as shown in Figure 4b for the last time step, starts
599 to emerge (Figure 9b). At 17:20 LST, the higher frequency for precipitation rates below 2
600 mm hr^{-1} in the control-b run, which is also described above as shown in Figure 4b for the
601 last time step, starts to show up, while the higher (lower) frequency for precipitation rates
602 higher than $\sim 12 \text{ mm hr}^{-1}$ (between ~ 2 and $\sim 12 \text{ mm hr}^{-1}$) in the control-b run, which is
603 established at 17:00 LST, maintains as time progresses from 17:00 LST to 17:20 LST
604 (Figure 9c). At 17:20 LST, the maximum precipitation rate increases to 42 (19) mm hr^{-1} in
605 the control-b (low-aerosol-b) run (Figure 9c). At 19:00 LST, the maximum precipitation
606 rate increases to ~ 45 (33) mm hr^{-1} for the control-b (low-aerosol-b) run, while the

607 qualitative nature of differences in the precipitation frequency distributions with the tipping
608 precipitation rates of ~ 2 and ~ 12 mm hr⁻¹ between the runs does not vary much between
609 17:20 and 19:00 LST (Figures 9c and 9d). The qualitative nature of differences in the
610 cumulative precipitation frequency between the runs and the maximum precipitation rates
611 in each of the runs, which are established at 19:00 LST, do not vary significantly until the
612 end of the simulation period (Figures 4b and 9d).

613

614 **b. Condensation, deposition, updrafts and associated variables**

615

616 As done for the Seoul case, as a way of better understanding differences in the cumulative
617 precipitation amount and frequency between the control-b and low-aerosol-b runs, the
618 evolutions of differences in the vertical distributions of the area-averaged condensation
619 rates, deposition rates, freezing rates, the mass density of each class of hydrometeors and
620 updrafts mass fluxes are obtained and shown in Figures 10. Cloud fractions are 0.12 (0.11),
621 0.25 (0.22), 0.36 (0.32), 0.43 (0.40) and 0.48 (0.47) in the control-b (low-aerosol-b) run at
622 14:20, 15:40, 16:00, 17:20 and 19:00 LST, respectively. Here, we see that cloud fraction
623 varies by ~ 2 -12% between the runs. In Figure 10, horizontal black lines represent the
624 altitudes of freezing and melting. As seen in Figure 3b, precipitation starts around 16:00
625 LST but differences in condensation rates start at 14:20 LST with higher condensation rates
626 in the control-b run (Figure 10a). Similar to the situation in the Seoul case, higher
627 concentrations of aerosols acting as CCN induce more nucleation of droplets, higher
628 CDNC and associated greater integrated surface of droplets in the control-b run. CDNC,
629 which is averaged over grid points and time steps with non-zero CDNC, is 992 and 341
630 cm⁻³ in the control-b and low-aerosol-b runs, respectively. Hence, more droplet surface is
631 provided for water vapor to condense onto in the control-b run. This leads to more
632 condensation in the control-b run. Due to this, cloud-liquid or droplet mass becomes greater
633 in the control-b run at 14:20 LST (Figure 10a). Increased condensation rates induce
634 increased condensational heating and thus intensified updrafts (Figure 10a). These
635 updrafts enable the maximum cloud depth to be ~ 12 km in the control-b run and this depth
636 is just ~ 1 % deeper than that in the low-aerosol-b run for the whole simulation period. This
637 negligible difference in the maximum cloud depth between the runs is due to the fact that

638 clouds with the maximum depth reach the tropopause in both of runs and thus there is not
639 much wiggle room to make significant differences in cloud depth between the runs.

640 When time reaches 15:40 LST, deposition rates and snow mass start to show
641 differences between the runs, while higher condensation rates and droplet mass maintain
642 in the control-b run with the time progress from 14:20 LST to 15:40 LST. However, unlike
643 the situation in the Seoul case, higher concentrations of aerosols acting as CCN result in
644 lower deposition rates and snow mass in the control-b run (Figure 10b). When time
645 progresses from 15:40 LST to 16:00 LST, differences in freezing start to occur and freezing
646 rates are lower (higher) at altitudes between ~6 and ~8 km (~4 and ~6 km), while higher
647 condensation rates and droplet mass, and lower snow mass maintain in the control-b run
648 (Figure 10c). Due to stronger updrafts, which are mainly ascribed to more condensation,
649 deposition rates start to be higher at altitudes between ~7 and ~9 km and freezing rates are
650 higher at altitudes between ~4 and ~6 km in the control-b run with the time progress from
651 15:40 LST to 16:00 LST (Figure 10c). Differences in freezing rates are similar to those in
652 deposition and ~two orders of magnitude smaller than those in condensation at 16:00 LST
653 (Figure 10c). At 16:00 LST, differences in hail mass between the runs appear up and hail
654 mass is slightly lower in the control-b run (Figure 10c). At 17:20 LST, overall, freezing
655 rates are lower at altitudes between ~4 and ~8 km, while overall, snow and hail mass is still
656 lower, and droplet mass is still higher in the control-b run (Figure 10d). Differences in
657 freezing rates are ~2 times smaller than those in deposition and ~one order of magnitude
658 smaller than those in condensation at 17:20 LST (Figure 10d). Due to more condensation
659 and droplet mass, greater raindrop mass appears up in the control-b run at 17:20 LST
660 (Figure 10d). As the time progresses to 19:00 LST, deposition rates become lower at the
661 altitudes from ~7 km to ~12 km and overall freezing rates become higher at altitudes from
662 ~4 km to ~10 km in the control-b run (Figure 10e). Overall, lower snow and hail mass
663 maintains in the control-b run as time progresses from 17:20 LST to 19:00 LST. As time
664 progresses from 17:20 LST to 19:00 LST, overall higher condensation rates, droplet and
665 raindrop mass maintain in the control-b run (Figure 10e). Here, while the time- and
666 domain-averaged deposition (condensation and freezing) rates are lower (higher) in the
667 control-b run over the whole simulation period, the average differences in freezing rates
668 are ~one to ~two orders of magnitude smaller than those in deposition and condensation

669 rates between the runs. Hence, more condensation (but not deposition and freezing) is a
670 main cause of stronger updrafts in the control-b run. More condensation and more freezing
671 tend to induce increases in the mass of precipitable hydrometeors in the control-b run. Less
672 deposition tends to induce decreases in the mass of precipitable hydrometeors in the
673 control-b run. This competition between condensation, deposition and freezing leads to
674 negligible differences in the cumulative precipitation amount at the last time step between
675 the control-b and low-aerosol-b runs, although roles of freezing in this competition are
676 negligible as compared to those of condensation and deposition.

677

678 **c. Condensation frequency distributions, horizontal distributions of**
679 **condensation and precipitation, and condensation-precipitation**
680 **correlations**

681

682 Figure 11 shows the horizontal distribution of the column-averaged condensation rates over
683 the domain and Figure 12 shows the cumulative frequency distributions of column-
684 averaged condensation rates at selected times. As in the Seoul case, the horizontal
685 distribution of condensation rates is superimposed on that of precipitation rates and the
686 terrain in Figure 11. At 14:20 LST, condensation starts to occur in places with mountains,
687 which induce forced convection, and condensation is concentrated around the center of the
688 domain as marked by a yellow circle (Figures 11a and 11b). Note that condensation does
689 not occur in the plain area which is the south of the 100-m terrain-height contour line
690 (Figures 11a and 11b). Due to higher concentrations of aerosols acting as CCN, there is
691 more condensation around the center in the control-b run than in the low-aerosol-b run
692 (Figures 11a and 11b). This leads to a situation where the control-b run has the higher area-
693 averaged condensation rates than the low-aerosol-b run (Figure 10a). Then, as time
694 progresses to 17:20 LST, the condensation area extends to the eastern and western parts of
695 the domain mostly over mountain areas (Figures 11c and 11d). Hence, the main source of
696 condensation is considered to be forced convection over mountains. As seen in Figures 11c
697 and 11d, higher concentrations of aerosols acting as CCN induce the control-b run to have
698 much more condensation spots and thus much bigger areas with condensation than the low-
699 aerosol-b run at 17:20 LST. Associated with this, CCN-induced more condensation in the

700 control-b run maintains with the time progress to 17:20 LST (Figure 10d). At 17:20 LST,
701 precipitation mainly occurs in a spot which is in the western part of areas with relatively
702 high condensation rates (Figures 11c and 11d).

703 At 17:20 LST, as seen in the cumulative frequency of condensation rates, the control-
704 b run has the higher condensation frequency above condensation rate of $\sim 10 \times 10^{-3} \text{ g m}^{-3} \text{ s}^{-1}$
705 ¹ and below that of $\sim 3 \times 10^{-3} \text{ g m}^{-3} \text{ s}^{-1}$ than the low-aerosol-b run (Figure 12a). This pattern
706 of differences in the condensation frequency distribution with the tipping condensation-
707 rate points at $\sim 10 \times 10^{-3}$ and $\sim 3 \times 10^{-3} \text{ g m}^{-2} \text{ s}^{-1}$ continues up to 19:00 LST (Figures 12b).
708 Figure 13 shows the mean precipitation rate over each of the column-averaged
709 condensation rates for the period up to 17:20 LST in the control-b run. A column-averaged
710 condensation rate in an air column with a precipitation rate at its surface is obtained and
711 these condensation and precipitation rates are paired at each column and time step. Then,
712 collected precipitation rates are classified and grouped based on the corresponding paired
713 column-averaged condensation rates. The classified precipitation rates corresponding to
714 each of the column-averaged condensation rates are averaged arithmetically to construct
715 Figure 13. There are only less than 10 % differences in the mean precipitation rate for each
716 of the column-averaged condensation rates between the control-b and low-aerosol-b runs
717 (not shown). Figure 13 shows that generally a higher condensation rate is related to a higher
718 mean precipitation rate. It is also roughly shown that, according to the mean precipitation
719 rate for each condensation rate, overall, condensation rates below $\sim 3 \times 10^{-3} \text{ g m}^{-3} \text{ s}^{-1}$ and
720 above $\sim 10 \times 10^{-3} \text{ g m}^{-3} \text{ s}^{-1}$ are correlated with precipitation rates below $\sim 2 \text{ mm hr}^{-1}$ and
721 above $\sim 12 \text{ mm hr}^{-1}$, respectively, while condensation rates between ~ 3 and $\sim 10 \times 10^{-3} \text{ g m}^{-3} \text{ s}^{-1}$
722 $\text{m}^{-3} \text{ s}^{-1}$ are correlated with precipitation rates between ~ 2 and $\sim 12 \text{ mm hr}^{-1}$ (Figure 13).
723 Hence, on average, the higher frequency of condensation with rates above $\sim 10 \times 10^{-3} \text{ g m}^{-3} \text{ s}^{-1}$
724 ³ s^{-1} and below $\sim 3 \times 10^{-3} \text{ g m}^{-3} \text{ s}^{-1}$ can be considered to lead to the higher frequency of
725 precipitation whose rates are higher than $\sim 12 \text{ mm hr}^{-1}$ and lower than $\sim 2 \text{ mm hr}^{-1}$ in the
726 control-b run, respectively. It can also be considered that the lower condensation frequency
727 between ~ 3 and $\sim 10 \times 10^{-3} \text{ g m}^{-3} \text{ s}^{-1}$ leads to the lower precipitation frequency between ~ 2
728 and $\sim 12 \text{ mm hr}^{-1}$ in the control-b run. It is found that this correspondence between
729 condensation and precipitation rates is valid whether analyses to construct Figure 13 are
730 repeated only for a time point at 16:30 LST or for a period between 16:30 and 17:00 LST.

731 These time point and period are related to analyses of the moist static energy as described
732 in Section e below.

733 At 17:20 LST, the larger precipitation frequency between ~ 2 and ~ 12 mm hr⁻¹ in the
734 low-aerosol-b run nearly offsets the larger precipitation frequency in the other ranges of
735 precipitation rates in the control-b run (Figure 9c). This leads to the similar average
736 precipitation rate between the runs at 17:20 LST and contributes to the similar cumulative
737 precipitation at the last time step between the runs (Figure 3b).

738

739 **d. Evaporation and gust fronts**

740

741 As time progresses from 17:00 to 19:00 LST, the precipitation system moves northward
742 (Figure 14). At the core of the precipitation system, due to evaporation and downdrafts,
743 there is the horizontal outflow forming at 17:00 LST (Figures 14a and 14b). The core is
744 represented by the field of precipitation whose rates are higher than 1 mm hr⁻¹ in Figure 14.
745 At the core, the northward outflow is magnified by the northward synoptic-scale wind,
746 while at the core, the outflow in the other directions is offset by the northward synoptic-
747 scale wind. Hence, the outflow is mainly northward from 17:00 LST onwards as marked
748 by yellow circles in Figures 14. This enables convergence or a gust front, which is produced
749 by the outflow from the core, to be mainly formed at the north of the core. Note that the
750 intensity of a gust front is proportional to that of outflow from a core of precipitation or
751 convective system (Weisman and Klemp, 1982; Houze, 1993). The strong gust front at the
752 north of the core generates strong updrafts, a significant amount of condensation and
753 precipitation. Then, a subsequent area with clouds and precipitation is formed at the north
754 of the core as time progresses, which means that the precipitation system extends or moves
755 to the north as seen in comparisons between sub-panels with different times in Figure 14.
756 This movement, which is induced by collaborative work between outflow, synoptic wind
757 and gust fronts, is typical in deep convective clouds.

758 As described above, the more droplet nucleation and greater integrated droplet surface
759 induce more condensation before 17:00 LST in the control-b run. This and lower efficiency
760 of collision and collection among droplets enable the control-b run to have a larger amount
761 of cloud liquid or droplets as a source of evaporation. This in turn enables more droplet

762 evaporation, more associated cooling and stronger downdrafts, although less rain
763 evaporation is in the control-b run particularly for the period from 17:00 LST to 19:00 LST.
764 The time- and domain-averaged droplet and rain evaporation rates are 0.72 (0.31) and 0.08
765 (0.13) $\text{g m}^{-3} \text{h}^{-1}$, respectively, while the time- and domain-averaged downdraft mass flux is
766 0.15 (0.10) $\text{kg m}^{-2} \text{s}^{-1}$ over the period from 17:00 LST to 19:00 LST in the control-b (low-
767 aerosol-b) run. More evaporation of droplets and associated stronger downdrafts with
768 higher concentrations of aerosols acting as CCN have been shown by the numerous
769 previous studies (e.g., Tao et al., 2007; Tao et al., 2012; Khain et al., 2008; Lee et al., 2018).

770 During the period between 17:00 and 19:00 LST, with the development of convergence
771 or the gust front, as mentioned above, the maximum precipitation rate increases from ~ 17
772 (17) to ~ 45 (33) mm hr^{-1} in the control-b (low-aerosol-b) run (Figure 9). This indicates
773 that the gust-front development contributes to the overall intensification of the precipitation
774 system, while it moves northward. If there were only northward synoptic-scale wind with
775 no formation of the gust front, the system would move northward with less intensification.
776 Over the period from 17:00 LST to 19:00 LST, stronger downdrafts and associated stronger
777 outflow generate a stronger gust front and more subsequent condensation in the control-b
778 run. This enhances the small initial difference, which is at 17:00 LST, in the frequency of
779 precipitation with rates above $\sim 12 \text{ mm hr}^{-1}$ between the runs substantially as time
780 progresses from 17:00 LST to 19:00 LST (Figure 9). Associated with this, with the time
781 progress, the nearly identical maximum precipitation rate between the runs at 17:00 LST
782 turns into the significantly higher maximum precipitation rate in the control-b run than in
783 the low-aerosol-b run (Figure 9). Around 19:00 LST, the system enters its dissipating stage,
784 accompanying reduction in the precipitating area and the area-averaged precipitation rate
785 (Figures 3b).

786

787 **e. Moist static energy**

788

789 Condensation, which controls droplet mass and precipitation, is controlled by updrafts and
790 updrafts are in turn controlled by instability. One of important factors that maintain
791 instability is the moist static energy. Motivated by this, to better understand differences in
792 the precipitation frequency distribution in association with those in the condensation

793 frequency distribution between the control-b and low-aerosol-b runs, we calculate the flux
 794 of the moist static energy and the flux is defined as follows:

795

$$796 \quad \vec{F}_S = S \times \rho \times \vec{V} \quad (1),$$

797

798 where \vec{F}_S represents the flux of the moist static energy, S the moist static energy, ρ the air
 799 density and \vec{V} the horizontal-wind vector. In Eq. (1), we see that the flux is in the vector
 800 form and has two components, which are its magnitude and direction. The fluxes of the
 801 moist static energy in the PBL are obtained over the domain at 16:30 LST, since in general,
 802 the moist static energy in the PBL has much stronger effects on instability and updrafts
 803 than that above the PBL. In particular, we focus on the PBL fluxes of the energy that cross
 804 the boundary over a time step at 16:30 LST between areas with the column-averaged
 805 condensation rate from $3 \times 10^{-3} \text{ g m}^{-3} \text{ s}^{-1}$ to $10 \times 10^{-3} \text{ g m}^{-3} \text{ s}^{-1}$, which are referred to as “area
 806 A”, and those with the column-averaged condensation rate above $10 \times 10^{-3} \text{ g m}^{-3} \text{ s}^{-1}$, which
 807 are referred to as “area B”. This is because we are interested in the exchange of the moist
 808 static energy between areas A and B and this exchange can be seen by looking at those
 809 fluxes which cross the boundary between those areas.

810 We are interested in the exchange of the energy, since we hypothesized that the
 811 exchange somehow alters instability in each of areas A and B in a way that there are
 812 increases (decreases) in instability, the updraft intensity, condensation and precipitation
 813 with increasing concentrations of aerosols acting as CCN in area B (A), leading to the
 814 higher (lower) frequency of condensation whose rates are higher than $10 \times 10^{-3} \text{ g m}^{-3} \text{ s}^{-1}$
 815 (between 3×10^{-3} and $10 \times 10^{-3} \text{ g m}^{-3} \text{ s}^{-1}$) and precipitation whose rates are higher than 12
 816 mm hr^{-1} (between 2 and 12 mm hr^{-1}) in the control-b run than in the low-aerosol-b run.
 817 When the PBL fluxes, which crosses the boundary over the time step at 16:30 LST, are
 818 summed at 16:30 LST, there is the net flux from area A to area B. This means that there is
 819 the net transportation of the moist static energy from areas with condensation rates between
 820 3×10^{-3} and $10 \times 10^{-3} \text{ g m}^{-3} \text{ s}^{-1}$ to those with condensation rates greater than $10 \times 10^{-3} \text{ g m}^{-3}$
 821 s^{-1} in the PBL at 16:30 LST as shown in Table 2. Table 2 shows the net summed flux of the
 822 moist static energy which crosses the boundary between areas A and B in the control-b run
 823 as well as the low-aerosol-b run. To calculate the net flux at 16:30 LST in Table 2, the

824 fluxes, which cross the boundary between areas A and B over the time step at 16:30 LST,
825 only at grid points in the PBL are summed. For the calculation, the flux from area A to area
826 B has a positive sign, while the flux from area B to area A has a negative sign. Since the
827 net flux is positive for both of the runs as shown in Table 2, there is the net flux from area
828 A to area B in the PBL. The above-described analysis for the fluxes crossing the boundary
829 between areas A and B is repeated for every time step between 16:30 and 17:00 LST and
830 based on this, the net summed flux over the period between 16:30 and 17:00 LST is
831 obtained. As shown in Table 2, the net flux for the period between 16:30 and 17:00 LST is
832 also positive as in the situation only for 16:30 LST. This means that there is the net
833 transportation of the moist static energy from area A to area B in the PBL during the period
834 between 16:30 and 17:00 LST.

835 At 16:30 LST, condensation with rates above $10 \times 10^{-3} \text{ g m}^{-3} \text{ s}^{-1}$ starts to develop and
836 this forms area B. Area B has stronger updrafts via greater condensational heating than in
837 other areas, including area A, with lower condensation rates. Stronger updrafts in area B
838 induce the convergence of air and associated moist static energy from area A to area B.
839 Since the average condensation rate and updrafts at 16:30 LST over area B are higher and
840 stronger due to increasing concentrations of aerosols acting as CCN, respectively, the air
841 convergence and the associated transportation of the moist static energy in the PBL from
842 area A to area B are stronger and more, respectively, in the control-b run than in the low-
843 aerosol-b run (Table 2). Stated differently, area B steals the moist static energy from area
844 A, and this occurs more effectively in the control-b run. This increases instability and
845 further intensifies updrafts in area B, and decreases instability and weakens updrafts in area
846 A, while these increases and decreases (intensification and weakening) of instability
847 (updrafts) are greater in the control-b run for the period from 16:30 LST to 17:00 LST.
848 This increases condensation, cloud mass and precipitation whose rates are higher than 12
849 mm hr^{-1} in area B, and decreases condensation, cloud mass and precipitation whose rates
850 are from 2 mm hr^{-1} to 12 mm hr^{-1} in area A. These increases and decreases occur more
851 effectively for the control-b run than for the low-aerosol-b run during the period. This in
852 turn leads to the lower precipitation frequency for the precipitation rates from 2 mm hr^{-1} to
853 12 mm hr^{-1} and the higher frequency for the precipitation whose rates are higher than 12
854 mm hr^{-1} at 17:00 LST in the control-b run (Figure 9b). The weakened updrafts and reduced

855 condensation turn a portion of precipitation with rates between 2 and 12 mm hr⁻¹ to
856 precipitation whose rates are below 2 mm hr⁻¹, and this takes place more efficiently in the
857 control-b run during the period between 16:30 and 17:00 LST. This eventually increases
858 the frequency of precipitation rates below 2 mm hr⁻¹ and this increase is greater for the
859 control-b run, leading to the greater precipitation frequency for the precipitation rates
860 below 2 mm hr⁻¹ in the control-b run at 17:20 LST (Figure 9c).

861

862 **5. Discussion**

863

864 **5.1 Comparison of the Seoul and Beijing cases**

865

866 In this section, we compare the Seoul case to the Beijing case. For the comparison,
867 remember that on average, a pair of the control-s and low-aerosol-s runs has the same
868 perturbation of aerosols acting as CCN as in a pair of the control-b and low-aerosol-b runs.
869 Associated with the fact that clouds in the Seoul case are less deep than those in the Beijing
870 case, overall, updrafts in the Seoul case are not as strong as those in the Beijing case. Hence,
871 unlike the situation in the Beijing case, stronger updrafts, which accompany higher
872 condensation rates, and associated convergence in the Seoul case are not strong enough to
873 steal the sufficient amount of the moist static energy from weaker updrafts which
874 accompany lower condensation rates. This makes the redistribution of the moist static
875 energy between areas with relatively higher condensation rates and those with relative
876 lower condensation rates, such as that between areas A and B for the Beijing case,
877 ineffective for the Seoul case. Due to this, the sign of CCN-induced changes in the
878 frequency of precipitation rates does not vary throughout all of the precipitation rates
879 except for the range of low precipitation rates where there are nearly no CCN-induced
880 changes in the frequency in the Seoul case as shown in Figure 4a. As seen in Figure 4a,
881 mainly due to increases in condensation and deposition, precipitation frequency increases
882 for most of precipitation rates, although the precipitation frequency does not show
883 significant changes as concentration of aerosols acting as CCN increases for relatively low
884 precipitation rates in the control-s run as compared to that in the low-aerosol-s run. This
885 means that there are no tipping precipitation rates where the sign of CCN-induced changes

886 in the frequency of precipitation rates changes in the Seoul case, contributing to the higher
887 cumulative precipitation amount in the simulation with higher concentrations of aerosols
888 acting as CCN for the Seoul case, which are different from the situation in the Beijing case.

889 In the Beijing case with deeper clouds as compared to those in the Seoul case, clouds
890 develop gust fronts via strong downdrafts and associated strong outflow. These gust fronts
891 play an important role in developing strong convection and associated high precipitation
892 rates. Unlike the situation in the Seoul case, there are strong clouds and associated updraft
893 entities that are able to steal heat and moisture (or the moist static energy) as sources of
894 instability from areas with relatively less strong clouds and updrafts with medium strength;
895 note that these strong clouds here involve stronger updrafts via greater condensational
896 heating as described in Section e above and this enables these clouds to be thicker and have
897 higher cloud mass than these less strong clouds. This further intensifies strong clouds and
898 weakens less strong clouds with medium strength. Due to this, the cumulative frequency
899 of heavy (medium) precipitation in association with strong clouds (less strong clouds with
900 medium strength) increases (decreases). Some of the weakened clouds eventually produce
901 light precipitation, which increase the cumulative frequency for light precipitation. The
902 intensification of strong clouds and the weakening of less strong clouds with medium
903 strength gets more effective with increasing concentration of aerosols acting as CCN.
904 Hence, in the Beijing case, for medium precipitation in association with less strong clouds,
905 the simulation with higher concentration of aerosols acting as CCN shows the lower
906 cumulative precipitation frequency at the last time step. However, for heavy precipitation,
907 which is associated with strong clouds, and light precipitation, the simulation with higher
908 concentrations of aerosols acting as CCN shows the higher cumulative precipitation
909 frequency at the last time step. These differential responses of precipitation to increasing
910 concentration of aerosols acting as CCN among different types of precipitation occur in the
911 circumstances of the similar cumulative precipitation amount between the simulations with
912 different concentration of aerosols acting as CCN. This similar precipitation amount is due
913 to above-mentioned competition between CCN-induced changes in condensation,
914 deposition and freezing.

915 In both of the Seoul and Beijing cases, CCN-induced changes in condensation plays an
916 important role in making differences in the precipitation amount and/or the precipitation

917 frequency distribution between the simulations with different concentration of aerosols
918 acting as CCN. It is notable that in less deep clouds in the Seoul case, in addition to
919 condensation, deposition plays a role in precipitation to induce CCN-induced increases in
920 the precipitation amount. CCN-induced increases in condensation initiate the differences
921 in cloud mass and precipitation and then CCN-induced increases in deposition follow to
922 further enhance those differences. In deep clouds in the Beijing case, condensation tends
923 to induce increases in cloud mass and precipitation, while deposition tends to induce
924 decreases in cloud mass and precipitation with increasing concentration of aerosols acting
925 as CCN. Hence, as clouds get shallower and thus ice processes become less active, the role
926 of deposition in CCN-induced changes in precipitation amount turns from CCN-induced
927 suppression of precipitation to enhancement of precipitation. Here, we find that contrary
928 to the traditional understanding, the role of variation of freezing, which is induced by the
929 varying concentration of aerosols acting as CCN but not INPs, in precipitation is negligible
930 as compared to that of condensation and deposition in both of the cases.

931

932 **6. Summary and conclusions**

933

934 This study examines impacts of aerosols, which act as CCN, on clouds and precipitation in
935 two metropolitan areas, which are the Seoul and Beijing areas, in East Asia that has
936 experienced substantial increases in aerosol concentrations over the last decades. The
937 examination is performed via simulations, which use a CSRM. These simulations are for
938 deep clouds which reach the tropopause in the Beijing case and for comparatively less deep
939 clouds which do not reach the tropopause yet grow above the level of freezing in the Seoul
940 case.

941 In both of the cases, CCN-induced changes in condensation plays a critical role in
942 CCN-induced variation of precipitation properties (e.g., the precipitation amount and the
943 precipitation frequency distribution). In the Seoul case, CCN-induced increases in
944 condensation and subsequent increases in deposition lead to CCN-induced increases in the
945 precipitation frequency over most of precipitation rates and thus in the precipitation amount.
946 However, in the Beijing case, while there are increases in condensation with increasing
947 CCN concentrations, there are decreases in deposition with increasing CCN concentrations.

948 This competition between increases in condensation and decreases in deposition leads to
949 negligible CCN-induced changes in cumulative precipitation amount in the Beijing case.
950 In both of the cases, CCN-induced changes in freezing are negligible as compared to those
951 in condensation and deposition. In the Beijing case, there is another competition for the
952 moist static energy among clouds with different updrafts and condensation. This
953 competition results in CCN-induced differential changes in the precipitation frequency
954 distributions. With clouds getting deeper from the Seoul case to the Beijing case, clouds
955 and associated updrafts, which are strong enough to steal the moist static energy from other
956 clouds and their updrafts, appear. This makes strong clouds stronger and clouds with
957 medium strength weaker. With higher CCN concentrations, strong clouds steal more
958 energy, and thus strong clouds become stronger and clouds with medium strength weaker
959 with a greater magnitude. As a result of this, there are more frequent heavy precipitation
960 (whose rates are higher than 12 mm hr^{-1}) and light precipitation (whose rates are lower than
961 2 mm hr^{-1}), and less frequent medium precipitation (with rates from 2 mm hr^{-1} to 12 mm
962 hr^{-1}) with increasing CCN concentrations in the Beijing case.

963 In both of the Seoul and Beijing cases, there are mountains and they play an important
964 role in how cloud and precipitation evolve with time and space. In both of the cases, the
965 precipitating system moves or expands over mountains which induce forced convection
966 and generate condensation. This important role of mountains and forced convection in the
967 formation and evolution of the precipitation system has not been examined much in the
968 previous studies of aerosol-cloud interactions, since many of those previous studies (e.g.,
969 Jiang et al., 2006; Khain et al., 2008; Li et al., 2011; Morrison et al., 2011) have dealt with
970 convective clouds that develop over plains and oceans. Hence, findings in this study, which
971 are related to mountain-forced convection and its interactions with aerosols, can be
972 complementary to those previous studies. Stated differently, this study can shed light on
973 our path to the understanding of aerosol-cloud interactions over more general domains not
974 only with no terrain but also with terrain.

975

976

977

978

979 **Code/Data source and availability**

980

981 Our private computer system stores the code/data which are private and used in this study.
982 Note that in particular, the stored PM data are provided by the Korea Environment
983 Cooperation in South Korea and State Key Laboratory of Severe Weather in China. Upon
984 approval from funding sources, the data will be opened to the public. Projects related to
985 this paper have not been finished, thus, the sources prevent the data from being open to the
986 public currently. However, if information on the data is needed, contact the corresponding
987 author Seoung Soo Lee (slee1247@umd.edu).

988

989 **Author contributions**

990 Essential initiative ideas are provided by SSL, KJH and KHS to start this work. Simulation
991 and observation data are analyzed by SSL, JC and GK. JU and YZ review the results and
992 contribute to their improvement. CHJ and JG perform additional simulations, which are
993 required by the review process, and their basic analyses. CHJ, SKS, YGL and NU provide
994 ideas to handle the reviewers' comments.

995

996 **Competing interests**

997 The authors declare that they have no conflict of interest.

998

999 **Acknowledgements**

1000 This study is supported by the National Research Foundation of Korea (NRF) grant funded
1001 by the Korea government (MSIT) (No. NRF2020R1A2C1003215 and No.
1002 2020R1A2C1013278), Basic Science Research Program through the NRF funded by the
1003 Ministry of Education (No. 2020R1A6A1A03044834) and the "Construction of Ocean
1004 Research Stations and their Application Studies" project funded by the Ministry of Oceans
1005 and Fisheries, South Korea. This study is also supported by the National Research
1006 Foundation of Korea (NRF) by FRIEND (Fine Particle Research Initiative in East Asia
1007 Considering National Differences) project through the National Research Foundation of
1008 Korea (NRF) funded by the Ministry of Science and ICT (2020M3G1A1114617), and the
1009 Korea Meteorological Administration Research and Development Program "Research on
1010 Weather Modification and Cloud Physics" under Grant (KMA2018-00224). Authors thank

1011 Danhong Dong at Chinese Academy of Sciences and Fang Wu at Beijing Normal
1012 University for their reviewing this paper.

1013

1014

1015

1016

1017

1018

1019

1020

1021

1022

1023

1024

1025

1026

1027

1028

1029

1030

1031

1032

1033

1034

1035

1036

1037

1038

1039

1040

1041

1042 **References**

1043

1044 Brown, A., Milton, S., Cullen, M., Golding, B., Mitchell, J., and Shelly, A.: Unified
1045 modeling and prediction of weather and climate: A 25-year journey, *Bull. Am*
1046 *Meteorol. Soc.* 93, 1865–1877, 2012.

1047 Chen, F., and Dudhia, J.: Coupling an advanced land-surface hydrology model with the
1048 Penn State-NCAR MM5 modeling system. Part I: Model description and
1049 implementation, *Mon. Wea. Rev.*, 129, 569–585, 2001.

1050 Dong, B., Wilcox, L. J., Highwood, E. J., and Sutton, R. T.: Impacts of recent decadal
1051 changes in Asian aerosols on the East Asian summer monsoon: roles of aerosol–
1052 radiation and aerosol–cloud interactions, *Clim. Dyn.*, 53, 3235–3256, 2019.

1053 Eun, S.-H., Kim, B.-G., Lee, K.-M., and Park, J.-S.: Characteristics of recent severe haze
1054 events in Korea and possible inadvertent weather modification, *SOLA*, 12, 32–36,
1055 2016.

1056 Fan, J., Yuan, T., Comstock, J. M., et al.: Dominant role by vertical wind shear in regulating
1057 aerosol effects on deep convective clouds, *J. Geophys. Res.*, 114,
1058 doi:10.1029/2009JD012352, 2009.

1059 Fouquart, Y., and Bonnel, B.: Computation of solar heating of the Earth's atmosphere: a
1060 new parameterization, *Beitr. Phys. Atmos.*, 53, 35–62, 1980.

1061 Ha, K.-J., Nam, S., Jeong, J.-Y., et al., Observations utilizing Korean ocean research
1062 stations and their applications for process studies, *Bull. Amer. Meteor. Soc.*, 100,
1063 2061–2075, 2019.

1064 Holben, B. N., Tanré, D., Smirnov, et al.: An emerging ground-based aerosol climatology:
1065 Aerosol optical depth from AERONET, *J. Geophys. Res.*, 106, 12067–12097, 2001.

1066 Houze, R. A., *Cloud dynamics*, Academic Press, 573 pp, 1993.

1067 Hwang, S.-O., and Lee, D.-K.: A study on the relationship between heavy rainfalls and
1068 associated low-level jets in the Korean peninsula, *J. Korean. Meteorol. Soc.*, 29, 133–
1069 146, 1993.

1070 Jiang, H., Xue, H., Teller, A., Feingold, G., and Levin, Z.: Aerosol effects on the lifetime
1071 of shallow cumulus, *Geophys. Res. Lett.*, 33, L14806, doi:10.1029/2006GL026024,
1072 2006.

- 1073 Kar, S. K., Lioi, Y.A., and Ha, K.-J. : Aerosol effects on the enhancement of cloud-to-
1074 ground lightning over major urban areas of South Korea, *Atmos. Res.* , 92, 80-87,
1075 2009.
- 1076 Khain, A., BenMoshe, N., and Pokrovsky, A.: Factors determining the impact of aerosols
1077 on surface precipitation from clouds: Attempt of classification, *J. Atmos. Sci.*, 65,
1078 1721-1748, 2008.
- 1079 Khain, A., Pokrovsky, A., Rosenfeld, D., Blahak, U., and Ryzhkoy, A.: The role of CCN in
1080 precipitation and hail in a mid-latitude storm as seen in simulations using a spectral
1081 (bin) microphysics model in a 2D dynamic frame, *Atmos. Res.*, 99, 129–146, 2011.
- 1082 Khain, A., Rosenfeld, D., and Pokrovsky, A.: Aerosol impact on the dynamics and
1083 microphysics of deep convective clouds, *Quart. J. Roy. Meteor. Soc.*, 131, 2639-266,
1084 2005.
- 1085 Khain, A. D., BenMoshe, N., and A. Pokrovsky, A.: Factors determining the impact of
1086 aerosols on surface precipitation from clouds: An attempt at classification, *J. Atmos.*
1087 *Sci.*, 65, 1721–1748, doi:10.1175/2007JAS2515.1, 2008.
- 1088 King, J.: Automatic weather stations, available at
1089 [https://web.archive.org/web/20090522121225/http://www.automaticweatherstation.c](https://web.archive.org/web/20090522121225/http://www.automaticweatherstation.com/index.html)
1090 [om/index.html](https://web.archive.org/web/20090522121225/http://www.automaticweatherstation.com/index.html), 2009.
- 1091 Koop, T., Luo, B. P., Tsias, A., and Peter, T.: Water activity as the determinant for
1092 homogeneous ice nucleation in aqueous solutions, *Nature*, 406, 611-614, 2000.
- 1093 Lebo, Z. J., and Morrison, H.: Dynamical effects of aerosol perturbations on simulated
1094 idealized squall lines, *Mon. Wea. Rev.*, 142, 991-1009, 2014.
- 1095 Lee, D.-K., Kim, H.-R., and Hong, S.-Y.: Heavy rainfall over Korea during 1980–1990.
1096 Korean, *J. Atmos. Sci.*, 1, 32–50, 1998.
- 1097 Lee, S., Ho, C.-H., Lee, Y. G., Choi, H.-J. and Song, C.-K.: Influence of transboundary air
1098 pollutants from China on the high-PM10 episode in Seoul, Korea for the period
1099 October 16–20, 2008. *Atmos. Environ.*, 77, 430–439, 2013.
- 1100 Lee, S. S., Donner, L. J., Phillips, V. T. J., and Ming, Y.: The dependence of aerosol effects
1101 on clouds and precipitation on cloud-system organization, shear and stability, *J.*
1102 *Geophys. Res.*, 113, D16202, 2008.
- 1103 Lee, S. S., Kim, B.-G., and Yum, S. S., et al.: Effect of aerosol on evaporation, freezing and

- 1104 precipitation in a multiple cloud system, *Clim. Dyn.*, 48, 1069-1087, 2016.
- 1105 Lee, S. S., Li, Z., Mok, J., et al.: Interactions between aerosol absorption, thermodynamics,
1106 dynamics, and microphysics and their impacts on clouds and precipitation in a
1107 multiple-cloud system, *Clim. Dyn.*, <https://doi.org/10.1007/s00382-017-3552-x>,
1108 2017.
- 1109 Lee, S. S., Kim, B.-G., Li, Z., Choi, Y.-S., Jung, C.-H., Um, J., Mok, J., and Seo, K.-H.:
1110 Aerosol as a potential factor to control the increasing torrential rain events in urban
1111 areas over the last decades, *Atmos. Chem. Phys.*, 18, 12531–12550,
1112 <https://doi.org/10.5194/acp-18-12531-2018>, 2018.
- 1113 Li, Z., Niu, F., Fan, J., Liu, Y., Rosenfeld, D., and Ding, Y.: Long-term impacts of aerosols
1114 on the vertical development of clouds and precipitation, *Nat. Geosci.*, 4, 888-894,
1115 2011.
- 1116 Lohmann, U. and Diehl, K.: Sensitivity studies of the importance of dust ice nuclei for the
1117 indirect aerosol effect on stratiform mixed-phase clouds, *J. Atmos. Sci.*, 63, 968-982,
1118 2006.
- 1119 Lu, Z., Zhang, Q., and Streets, D. G.: Sulfur dioxide and primary carbonaceous aerosol
1120 emissions in China and India, 1996–2010, *Atmos. Chem. Phys.*, 11, 9839–9864, 2011.
- 1121 Mlawer, E. J., Taubman, S. J., Brown, P. D., Iacono, M. J., and Clough, S. A.: RRTM, a
1122 validated correlated-k model for the longwave, *J. Geophys. Res.*, 102, 16663-1668,
1123 1997.
- 1124 Möhler, O., et al, Efficiency of the deposition mode ice nucleation on mineral dust particles,
1125 *Atmos. Chem. Phys.*, 6, 3007-3021, 2006.
- 1126 Morrison, H., and Grabowski, W. W.: Cloud-system resolving model simulations of aerosol
1127 indirect effects on tropical deep convection and its thermodynamic environment,
1128 *Atmos. Chem. Phys.*, 11, 10503–10523, 2011.
- 1129 Oh, H., Ha, K.-J. and Timmermann, A.: Disentangling Impacts of Dynamic and
1130 Thermodynamic Components on Late Summer Rainfall Anomalies in East Asia, *J.*
1131 *Geophys. Res.*, 123, 8623-8633, 2018.
- 1132 Oh, H.-R., Ho, C.-H., Kim, J., Chen, D., Lee, S., Choi, Y.-S., Chang, L.-S., and Song, C.-
1133 K.: Long-range transport of air pollutants originating in China: A possible major cause
1134 of multi-day high-PM10 episodes during cold season in Seoul, Korea. *Atmos.*

- 1135 Environ., 109, 23–30, 2015.
- 1136 Pruppacher, H. R. and Klett, J. D.: Microphysics of clouds and precipitation, 714pp, D.
1137 Reidel, 1978.
- 1138 Rosenfeld, D., Lohmann, U., Raga, G. B., et al.: Flood or drought, How do aerosols affect
1139 precipitation? *Science*, 321, 1309-1313, 2008.
- 1140 Storer, R. L., van den Heever, S. C., and Stephens, G. L.: Modeling aerosol impacts on
1141 convection under differing storm environments, *J. Atmos. Sci.*, 67, 3904-3915, 2010.
- 1142 Seo, K.-H., Son, J. H., Lee, J.-H., and Park, H.-S.: Northern East Asian monsoon
1143 precipitation revealed by air mass variability and its prediction, *J. Clim.*, 28, 6221-
1144 6233, 2013.
- 1145 Tao, W.-K., Chen, J.-P., Li, Z., Wang, C., and Zhang, C.: Impact of aerosols on convective
1146 clouds and precipitation, *Rev. Geophys.*, 50, RG2001, 2012.
- 1147 Tao, W. K., Cloud resolving modeling, *J. Meteorol. Soc. Jpn.*, 85B, 305–330,
1148 doi:10.2151/jmsj.85B.305, 2007.
- 1149 van den Heever, S. C., Carrió, G. G., Cotton, W. R., DeMott, P. J., and Prenni, A. J.:
1150 Impacts of nucleating aerosol on Florida storms. part I: Mesoscale simulations, *J.*
1151 *Atmos. Sci.*, 63, 1752–1775, 2006.
- 1152 Wang, H., Skamarock, W. C., and Feingold, G.: Evaluation of scalar advection schemes in
1153 the Advanced Research WRF model using large-eddy simulations of aerosol-cloud
1154 interactions, *Mon. Wea. Rev.*, 137, 2547-2558, 2009.
- 1155 Weisman, M. L., and Klemp, J. B.: The dependence of numerically simulated convective
1156 storms on vertical wind shear and buoyancy, *Mon. Wea. Rev.*, 110, 504-520, 1982.
- 1157
- 1158
- 1159
- 1160
- 1161
- 1162
- 1163
- 1164
- 1165
- 1166
- 1167
- 1168
- 1169

1170 **FIGURE CAPTIONS**

1171

1172 Figure 1. Inner rectangles in (a) and (b) mark the Seoul area in the Korean Peninsula and
1173 the Beijing area in the East-Asia continent, respectively. A dot outside the inner rectangle
1174 in (a) marks Baekryongdo island. Dots in the inner rectangles in (a) and (b) mark the
1175 selected locations where precipitation and aerosol mass are measured. In (a) and (b), the
1176 light blue represents the ocean and the green the land area.

1177

1178 Figure 2. Time series of $PM_{2.5}$ observed at the ground station in Baekryongdo island (blue
1179 line) and of the average $PM_{2.5}$ over ground stations in the Seoul area (red line) between
1180 07:00 LST on December 22nd and 21:00 LST on December 24th in 2017. Note that $PM_{2.5}$
1181 observed at stations in the Seoul area is applied to the control-s run whose period is marked
1182 by the dashed rectangle. Time series of the average $PM_{2.5}$ over stations in the Seoul area in
1183 the low-aerosol-s run for the simulation period is also shown (black solid line).

1184

1185 Figure 3. Time series of precipitation rates at the surface, which are averaged over the
1186 domain and smoothed over 1 hour, (a) for the control-s and low-aerosol-s runs in the Seoul
1187 area and (b) for the control-b and low-aerosol-b runs in the Beijing area. In (a) and (b), the
1188 averaged and observed precipitation rates over the observation sites in the Seoul and
1189 Beijing areas, respectively, are also shown.

1190

1191 Figure 4. Observed and simulated cumulative frequency distributions of precipitation rates
1192 at the surface for (a) the Seoul case, which are collected over the Seoul area, and (b) the
1193 Beijing case, which are collected over the Beijing area, at the last time step. Simulated
1194 distributions are in the control-s and low-aerosol-s runs for the Seoul case and in the
1195 control-b and low-aerosol-b runs for the Beijing case. The observed distribution is obtained
1196 by interpolating and extrapolating the observed precipitation rates to grid points and time
1197 steps in the control-s and control-b runs for the Seoul and Beijing cases, respectively.

1198

1199 Figure 5. Cumulative frequency distributions of the precipitation rates at the surface in the
1200 control-s and low-aerosol-s runs for the Seoul case at (a) 06:00, (b) 10:00 and (c) 12:00
1201 LST.

1202

1203 Figure 6. Vertical distributions of differences in the area-averaged condensation,
1204 deposition and freezing rates, and cloud-liquid, raindrop, snow and hail mass density, and
1205 updraft mass fluxes between the control-s and low-aerosol-s runs at (a) 03:20, (b) 03:40,
1206 (c) 06:00 and (d) 12:00 LST. The horizontal black line in each panel represents the altitude
1207 of freezing or melting. Here, for the sake of the display brevity, snow mass density includes
1208 ice-mass density, while hail mass density includes graupel mass density.

1209

1210 Figure 7. Spatial distributions of terrain heights, column-averaged condensation rates,
1211 surface wind vectors and precipitation rates at (a) and (b) 03:40, (c) and (d) 08:40, (e) and
1212 (f) 10:00, and (g) and (h) 12:00 LST. The distributions in the control-s run are shown in (a),
1213 (c), (e) and (g), and the distributions in the low-aerosol-s run are shown in (b), (d), (f) and
1214 (h). Condensation rates are shaded. Dark-yellow and dark-red contours represent
1215 precipitation rates at 0.5 and 3.0 mm hr⁻¹, respectively, while beige, light brown and brown
1216 contours represent terrain heights at 100, 300 and 600 m, respectively. See text for yellow
1217 rectangles in (a), (b), (e) and (f).

1218

1219 Figure 8. Cumulative frequency distributions of the column-averaged condensation rates
1220 in the control-s and low-aerosol-s runs for the Seoul case at (a) 07:20 and (b) 09:00 LST.

1221

1222 Figure 9. Cumulative frequency distributions of the precipitation rates at the surface in the
1223 control-b and low-aerosol-b runs for the Beijing case at (a) 16:00, (b) 17:00, (c) 17:20, and
1224 (d) 19:00 LST.

1225

1226 Figure 10. Same as Figure 6 but for differences between the control-b and low-aerosol-b
1227 runs at (a) 14:20, (b) 15:40, (c) 16:00, (d) 17:20 and (e) 19:00 LST.

1228

1229 Figure 11. Spatial distributions of terrain heights, column-averaged condensation rates,
1230 surface wind vectors and precipitation rates at (a) and (b) 14:20, and (c) and (d) 17:20 LST.
1231 (a) and (c) are for the control-b run and (b) and (d) are for the low-aerosol-b run.
1232 Condensation rates are shaded. Dark-yellow and dark-red contours represent precipitation
1233 rates at 1.0 and 2.0 mm hr⁻¹, respectively, while beige, light brown, brown and dark brown
1234 contours represent terrain heights at 100, 500, 1000 and 1500 m, respectively. See text for
1235 yellow circles in (a) and (b).

1236

1237 Figure 12. Cumulative frequency distributions of the column-averaged condensation rates
1238 in the control-b and low-aerosol-b runs for the Beijing case at (a) 17:20 and (b) 19:00 LST.

1239

1240 Figure 13. Mean precipitation rates corresponding to each column-averaged condensation
1241 rate for the period between 14:00 and 17:20 LST in the control-b run. One standard
1242 deviation of precipitation rates is represented by a vertical bar at each condensation rate.

1243

1244 Figure 14. Spatial distributions of precipitation rates (shaded) and wind vectors (arrows)
1245 for the Beijing case at (a) and (b) 17:00, and (c) and (d) 19:00. The distributions in the
1246 control-b run are in (a) and (c). The distributions in the low-aerosol-b run are in (b) and (d).

1247

1248

1249

1250

1251

1252

1253

1254

1255

1256

1257

1258

Simulations	Site	Concentrations of background aerosols acting as CCN
Control-s run	Seoul area	Observed and affected by the aerosol advection
Low-aerosol-s run	Seoul area	Same as those in the control-s run but unaffected by the aerosol advection
Control-b run	Beijing area	Observed
Low-aerosol-b run	Beijing area	Reduced by a factor of 3.1 as compared to those observed

1259

1260 Table 1. Summary of simulations

1261

1262

Simulations	The net flux of the moist static energy which crosses the boundary between areas A and B ($\text{J m}^{-2} \text{ s}^{-1}$)	
	At 16:30 LST	16:30 to 17:00 LST
Control-b run	1.57×10^{12}	1.07×10^{15}
Low-aerosol-b run	1.15×10^{12}	7.55×10^{14}

1263

1264 Table 2. The net flux of the moist static energy which crosses the boundary between areas

1265 A and B at 16:30 LST and for a period from 16:30 to 17:00 LST.

1266

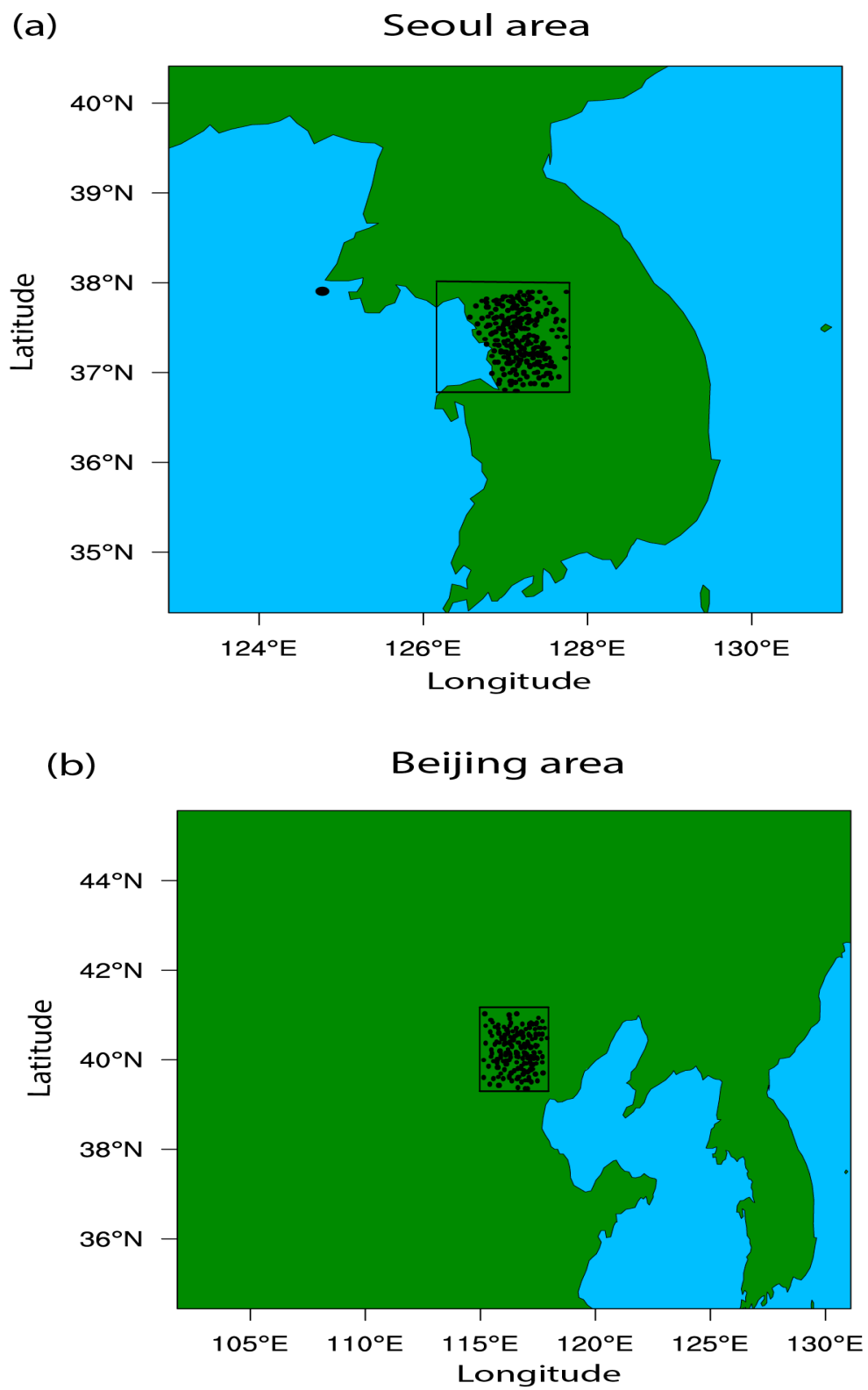
1267

1268

1269

1270

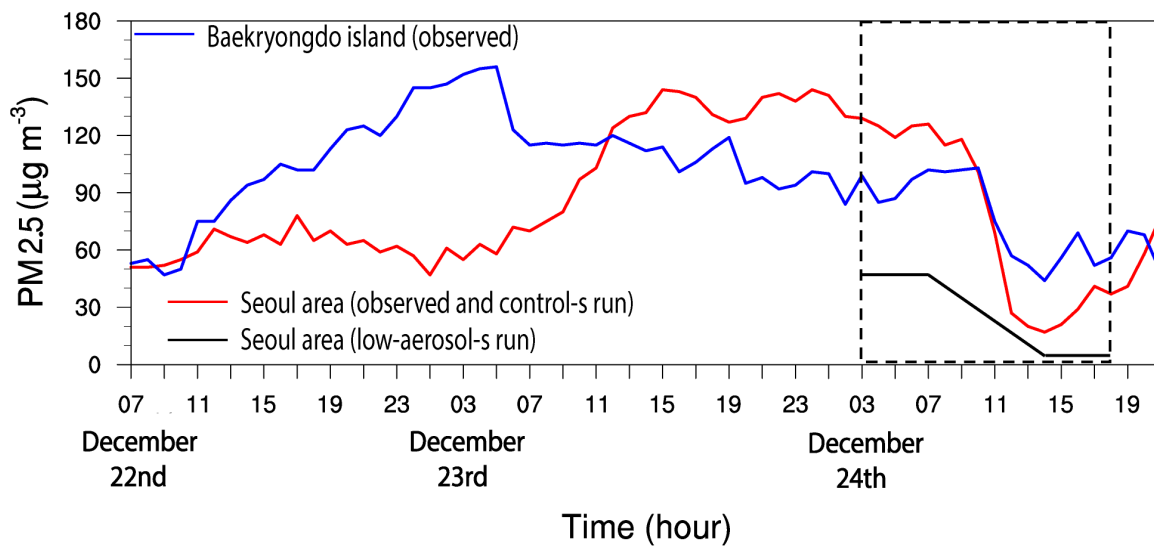
1271



1272

1273

Figure 1



1274

1275

1276

1277

1278

1279

1280

1281

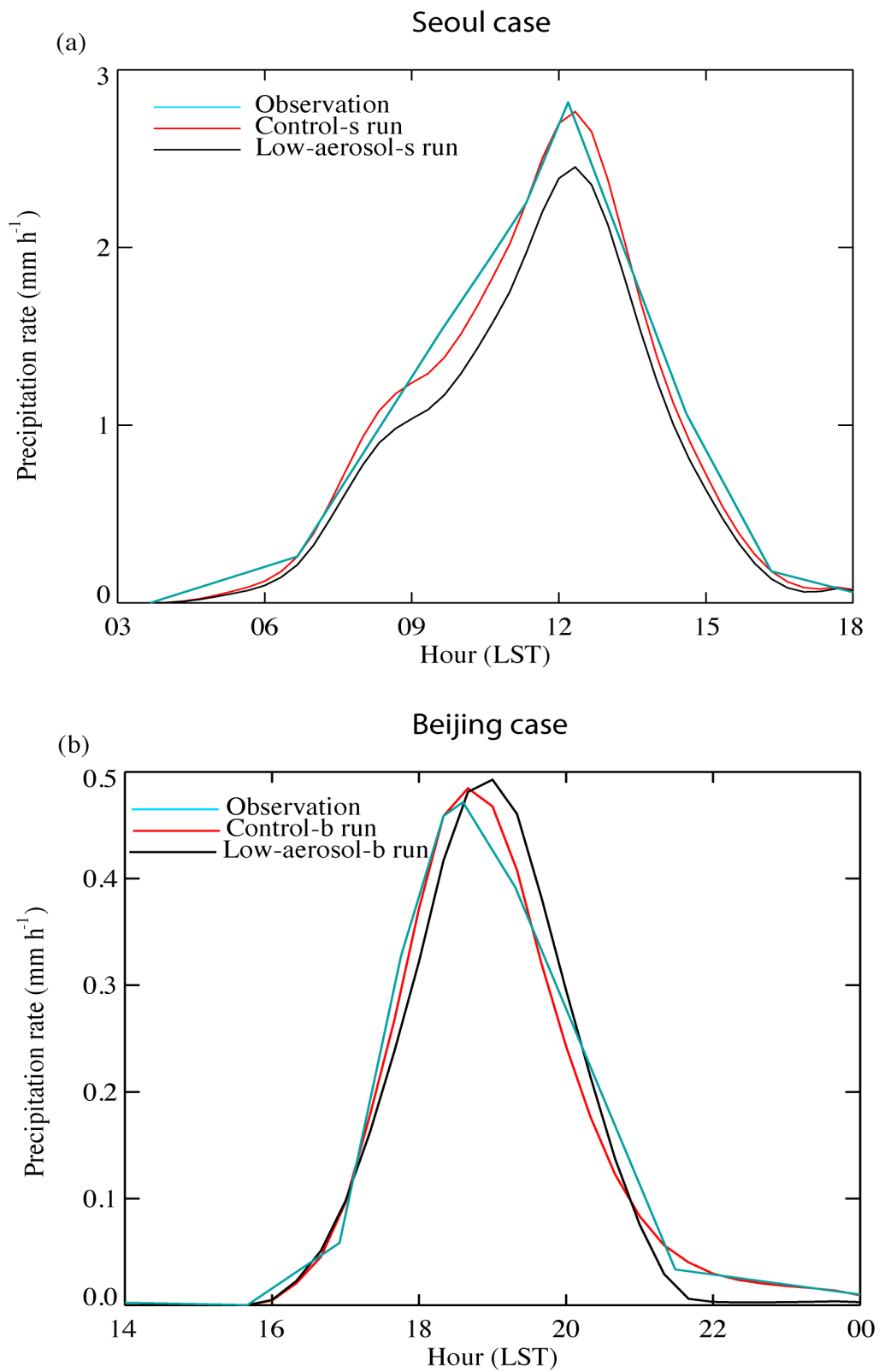
1282

1283

1284

1285

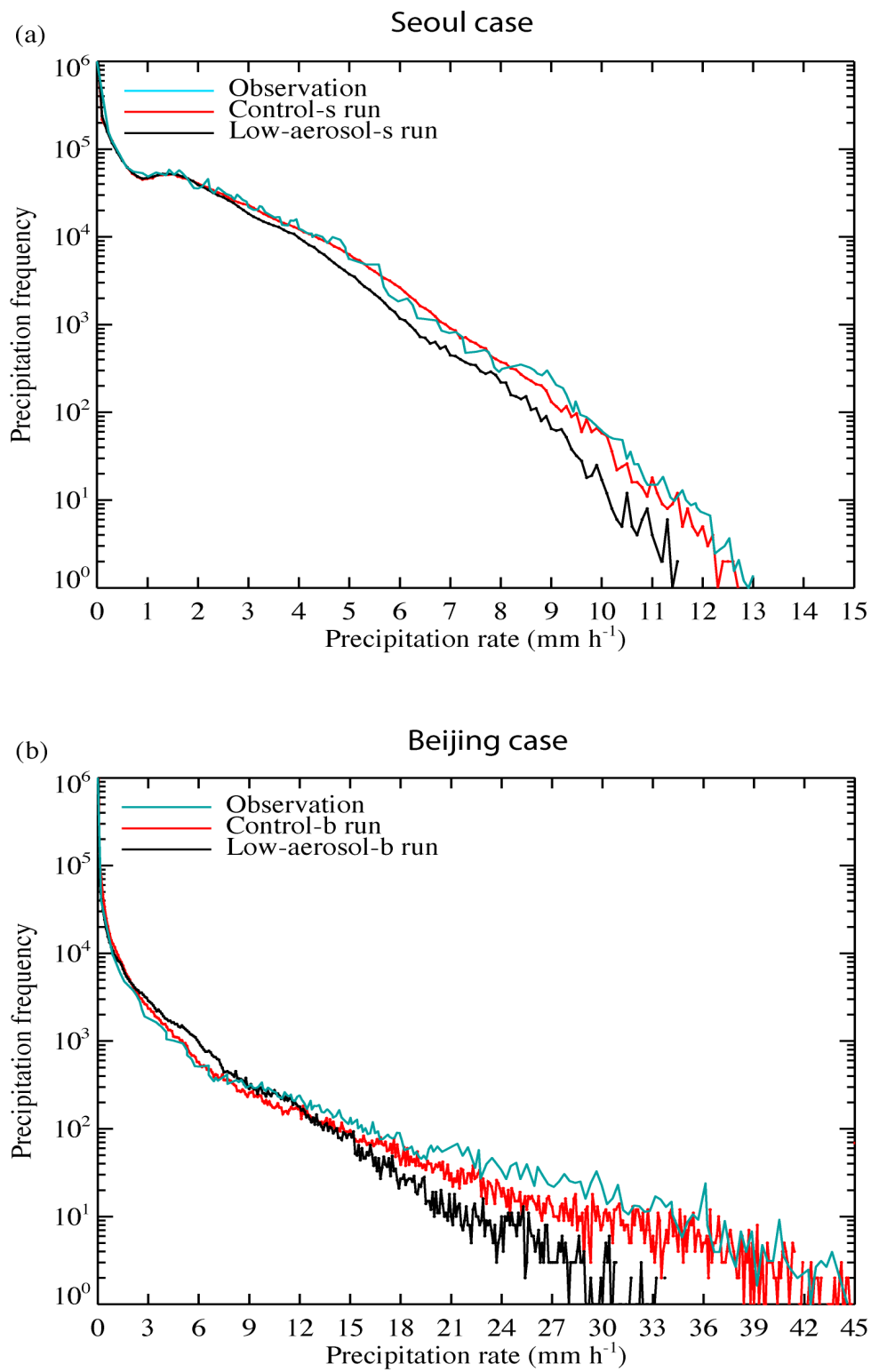
Figure 2



1286

1287

Figure 3

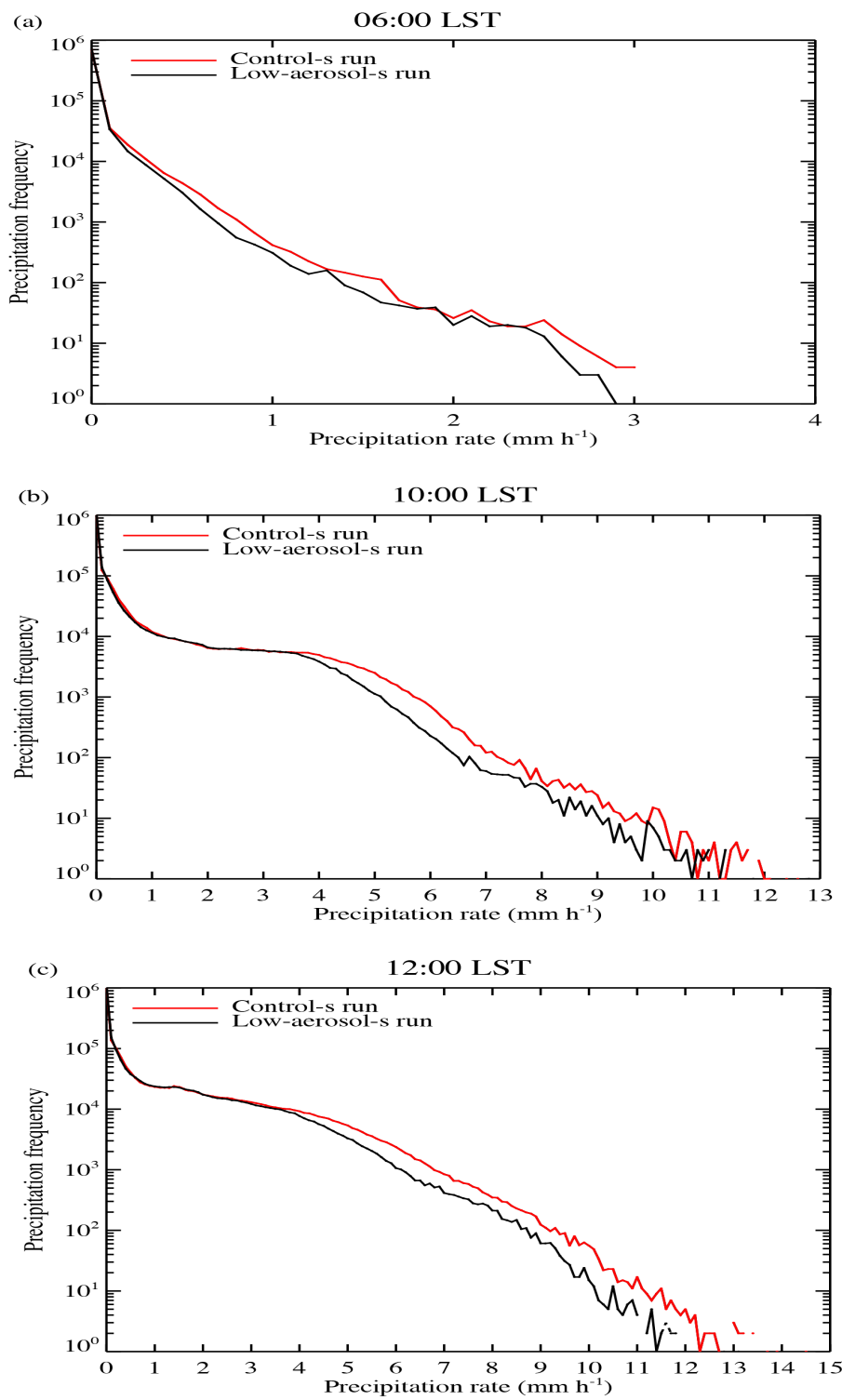


1288

1289

Figure 4

Seoul case

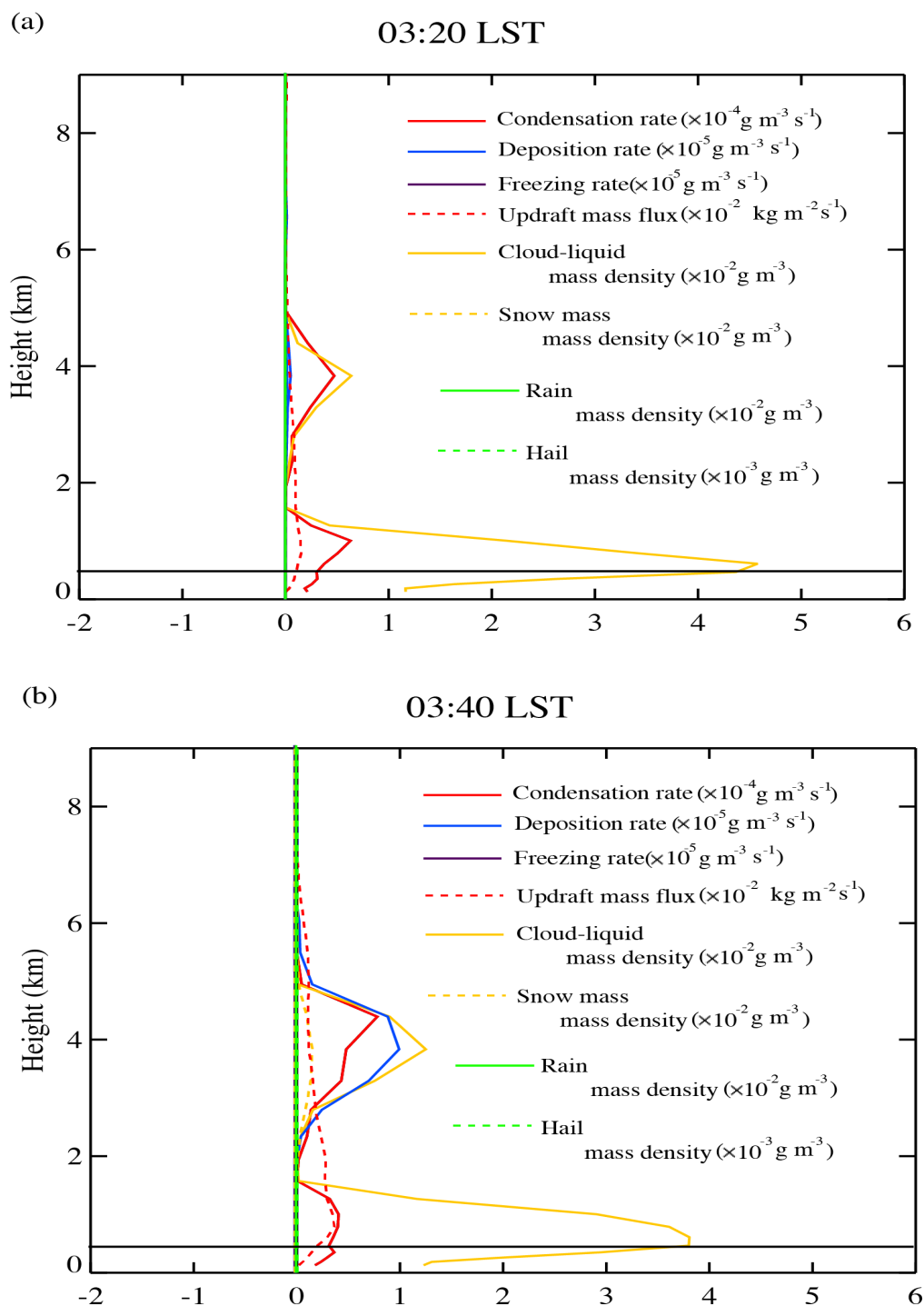


1290

1291

Figure 5

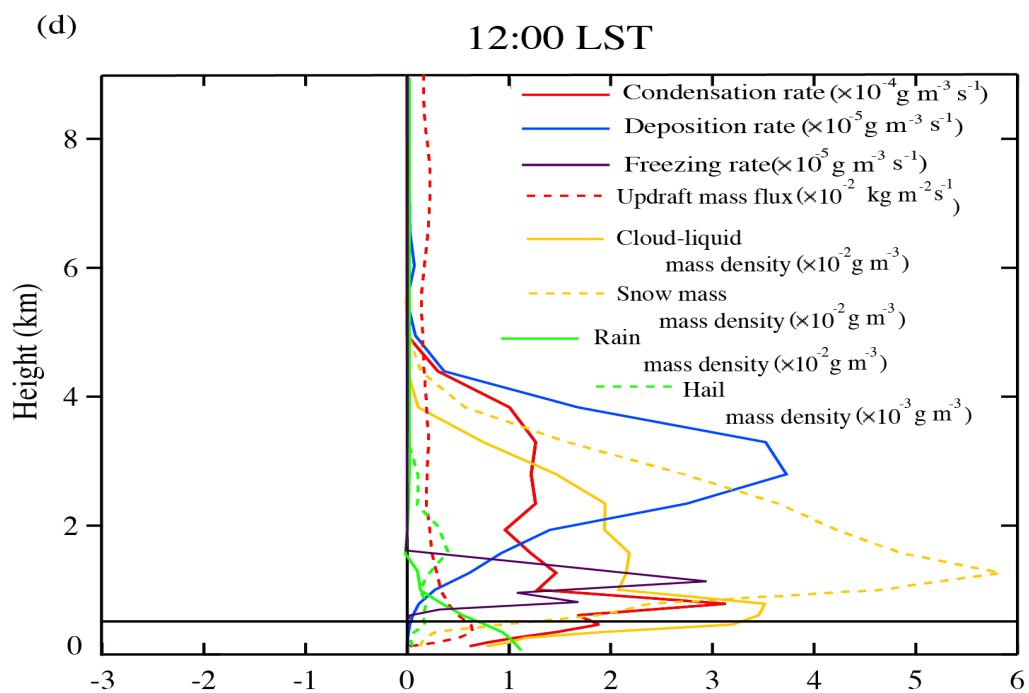
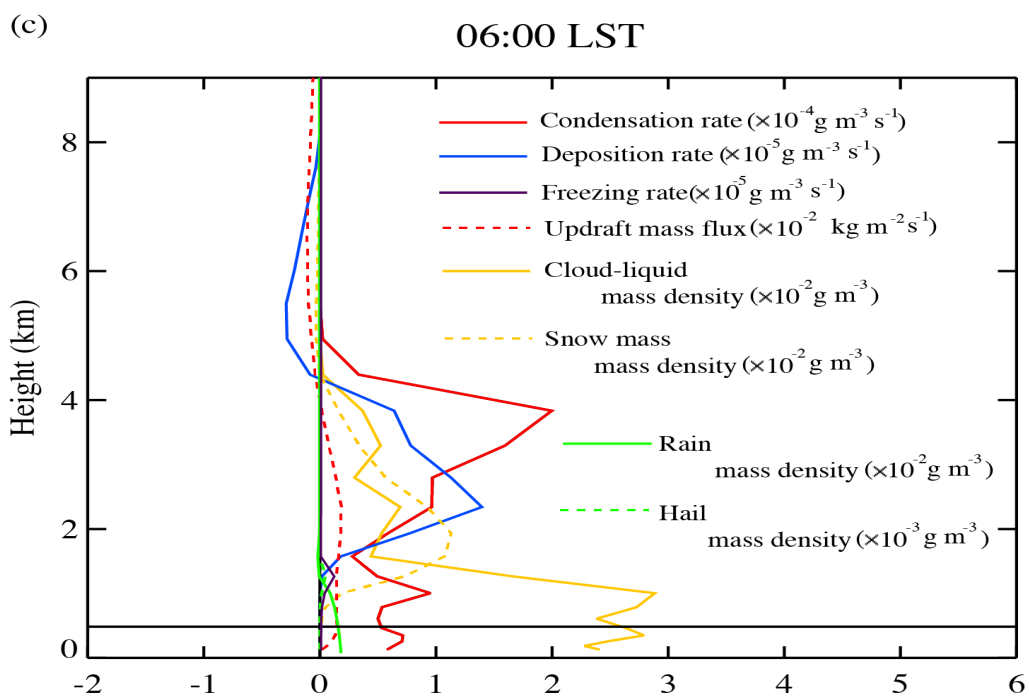
Seoul case (control-s run minus low-aerosol-s run)



1292

1293

Figure 6

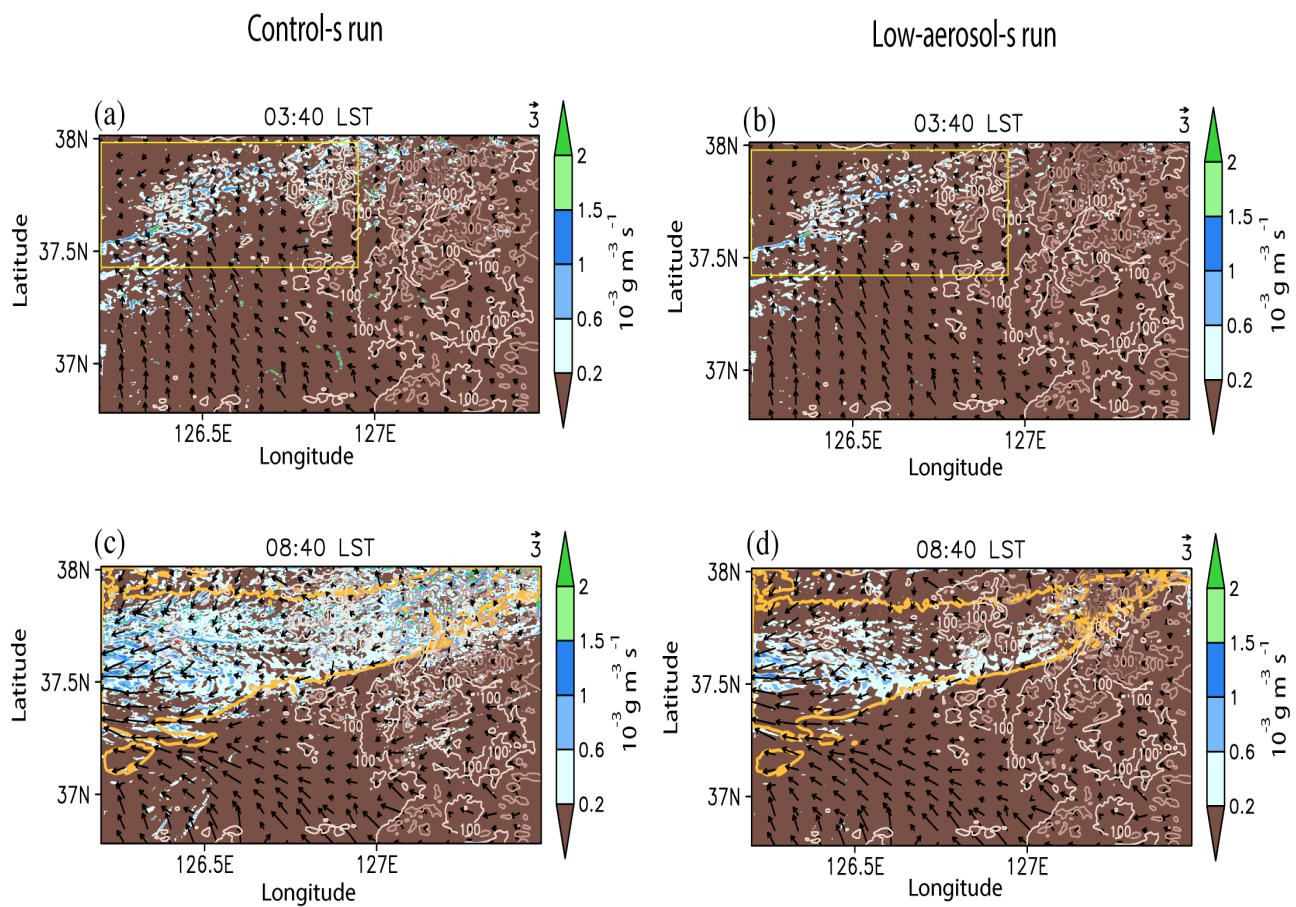


1294

1295

1296

Figure 6



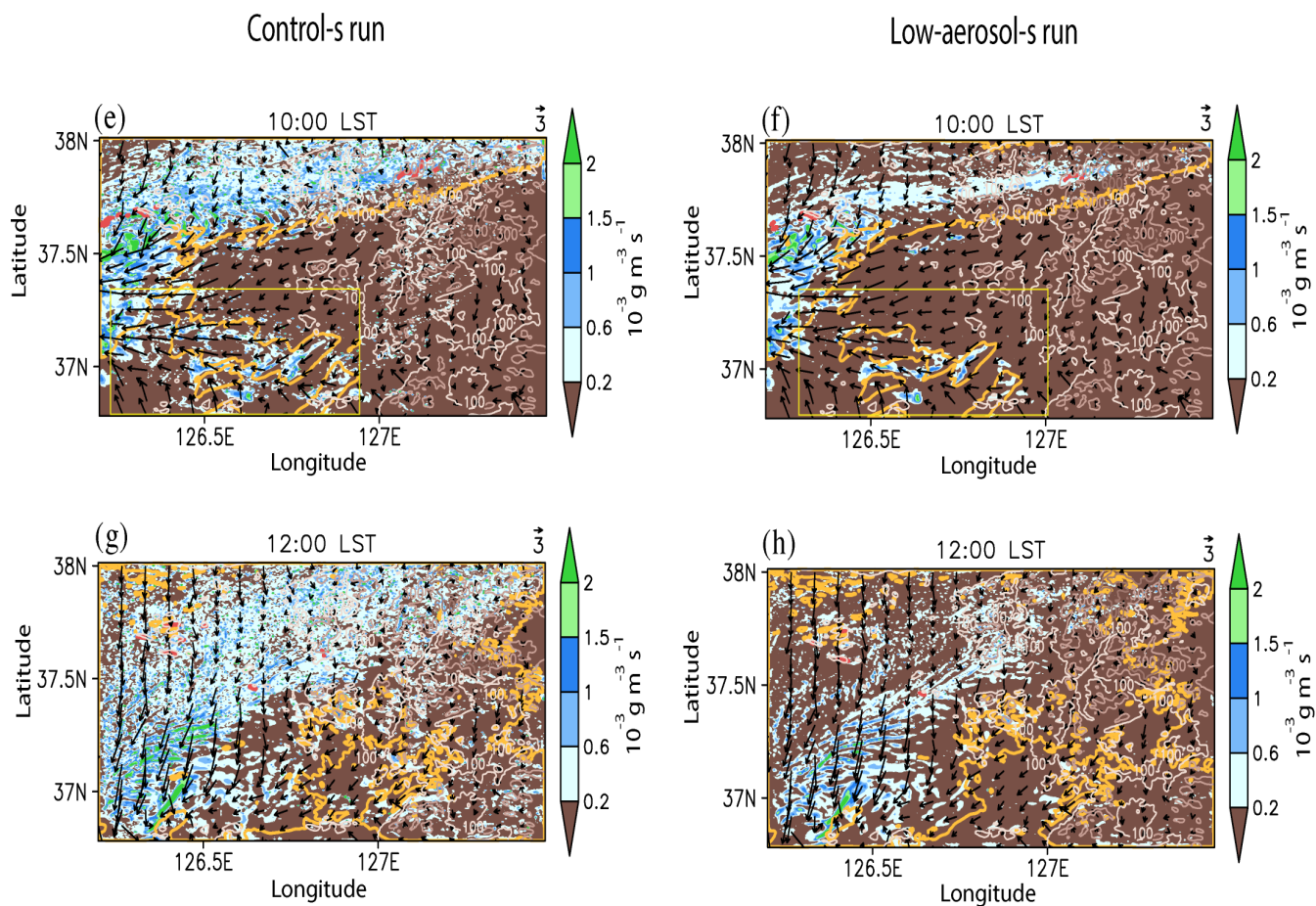
1297

1298

1299

1300

Figure 7



1301

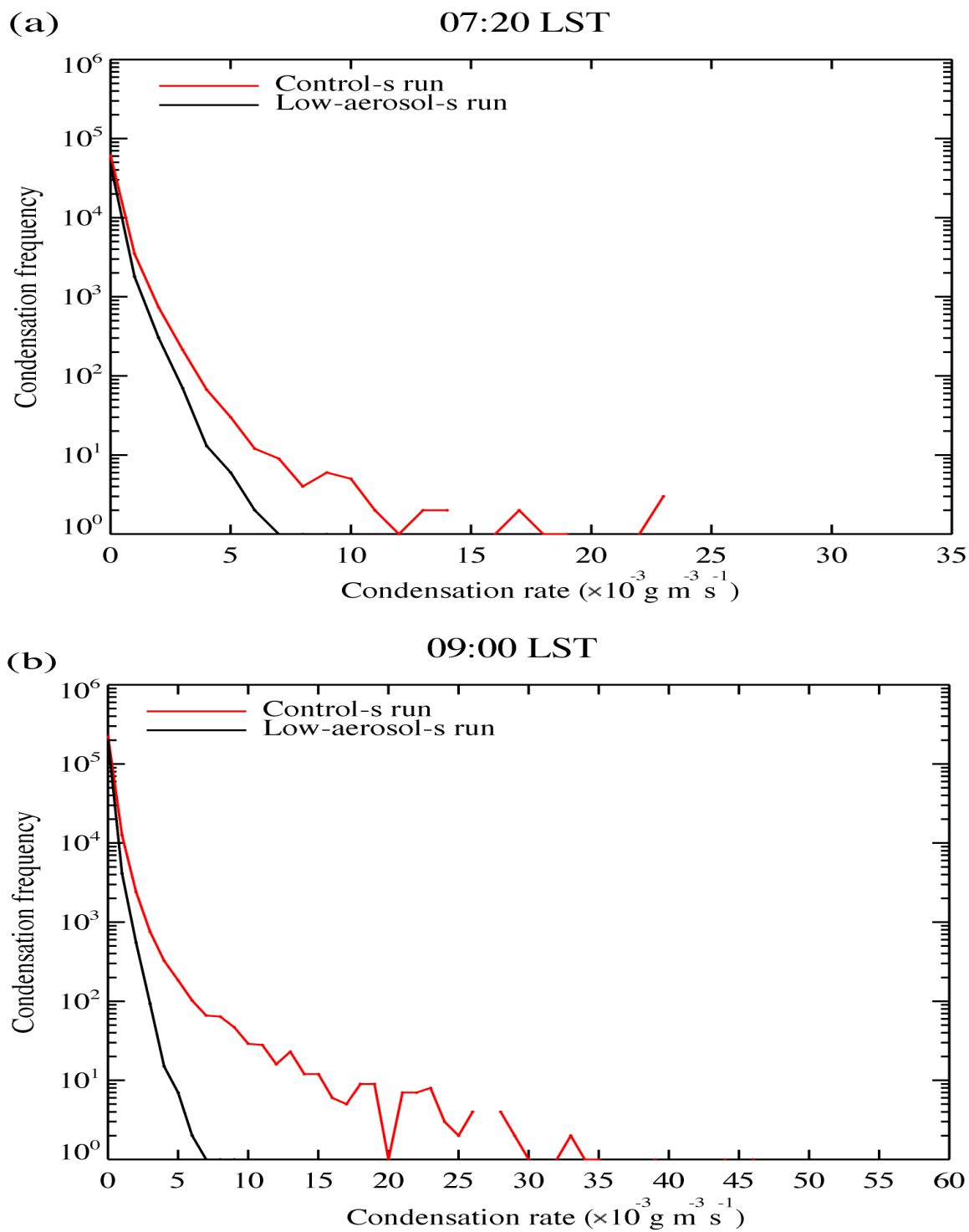
1302

1303

1304

Figure 7

Seoul case



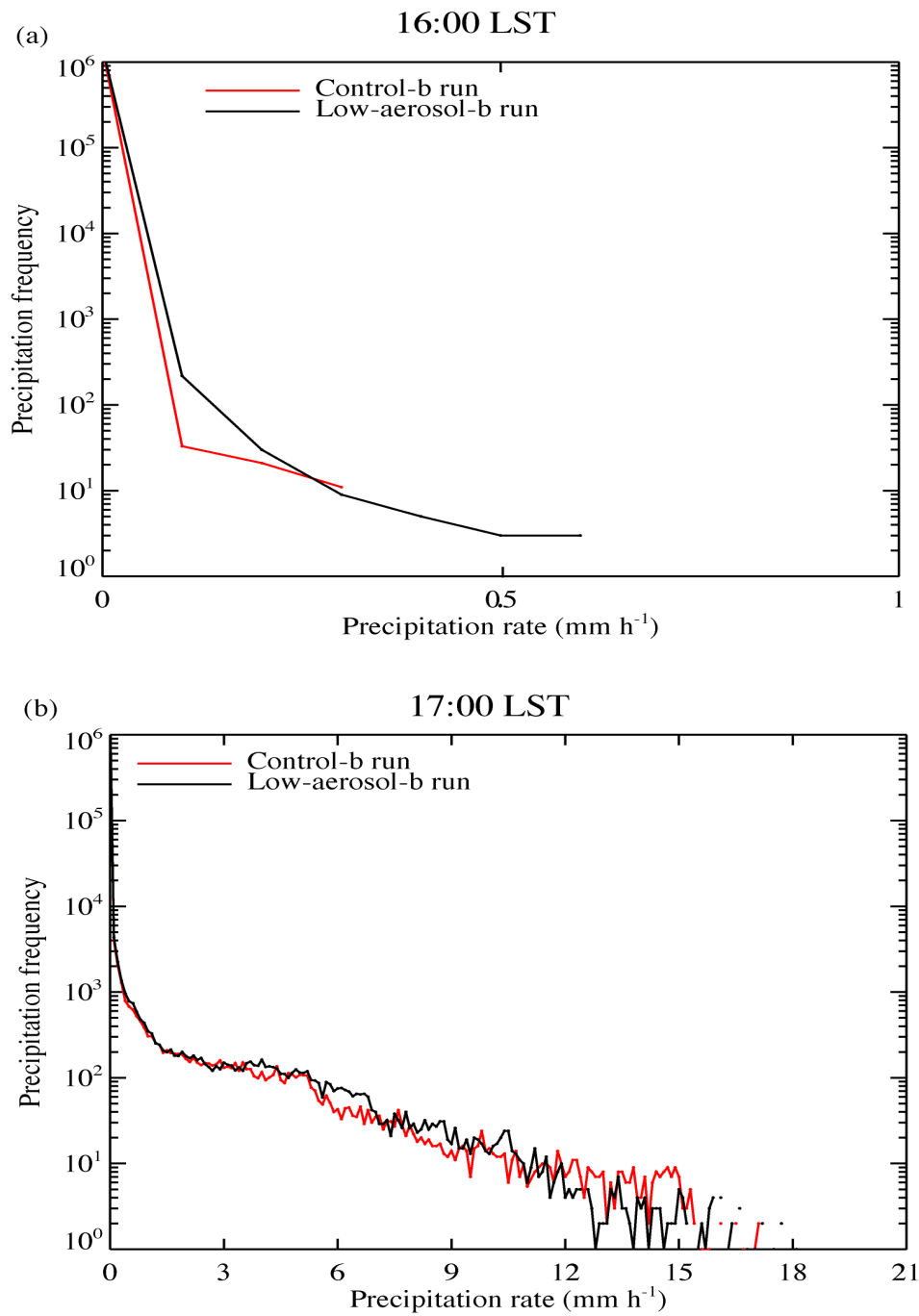
1305

1306

1307

Figure 8

Beijing case

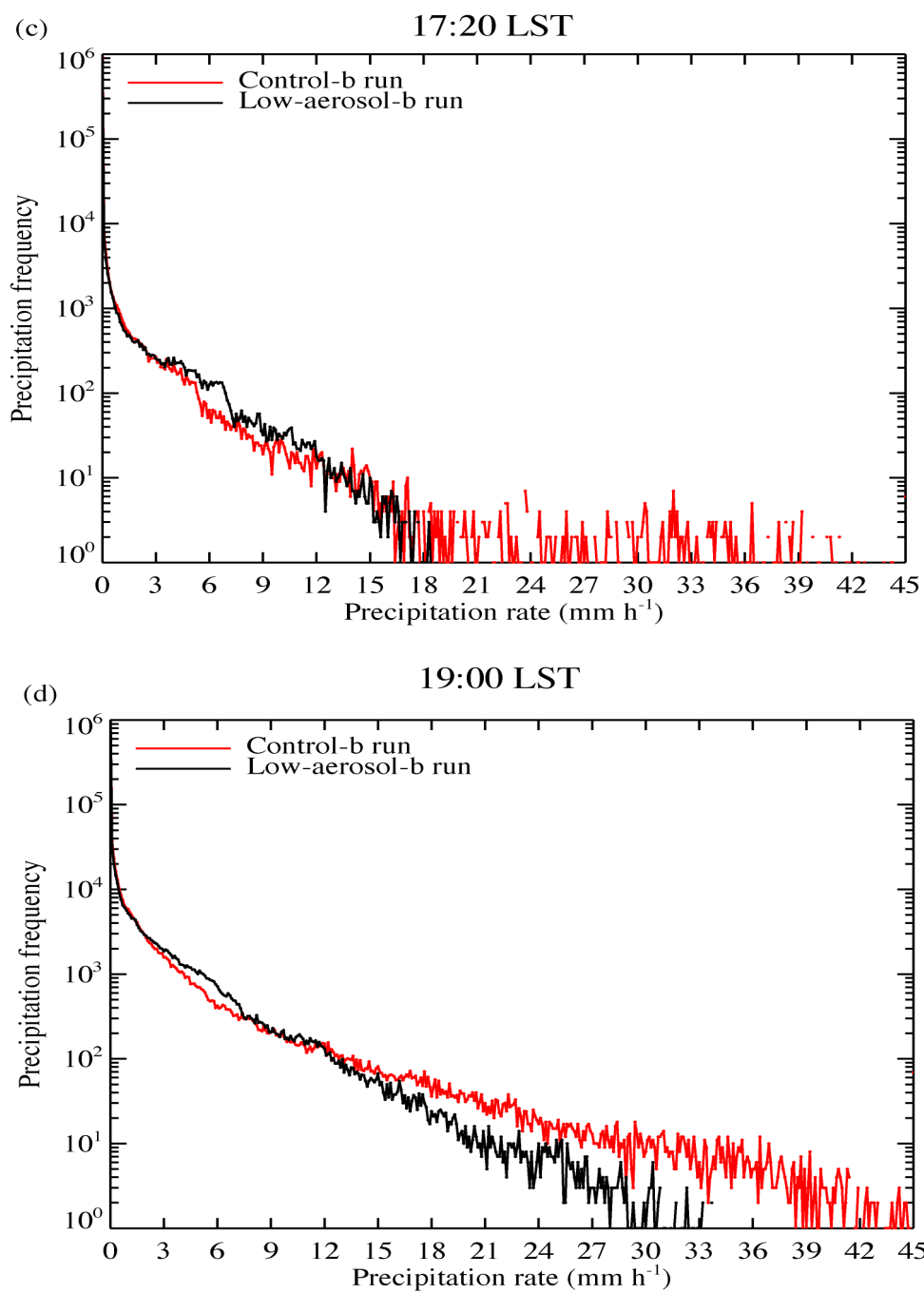


1308

1309

1310

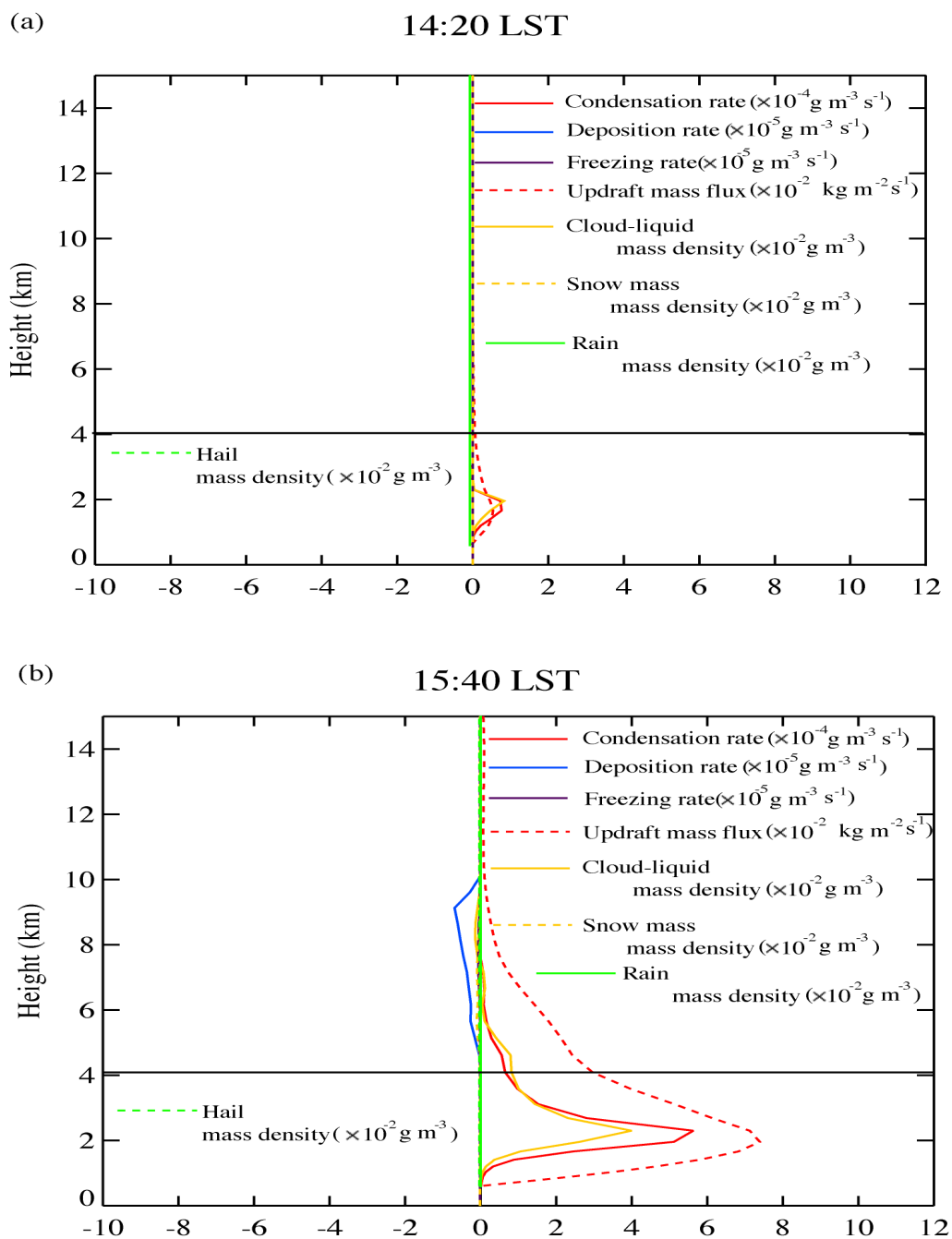
Figure 9



1311
1312
1313
1314
1315
1316

Figure 9

Beijing case (control-b run minus low-aerosol-b run)



1317

1318

Figure 10

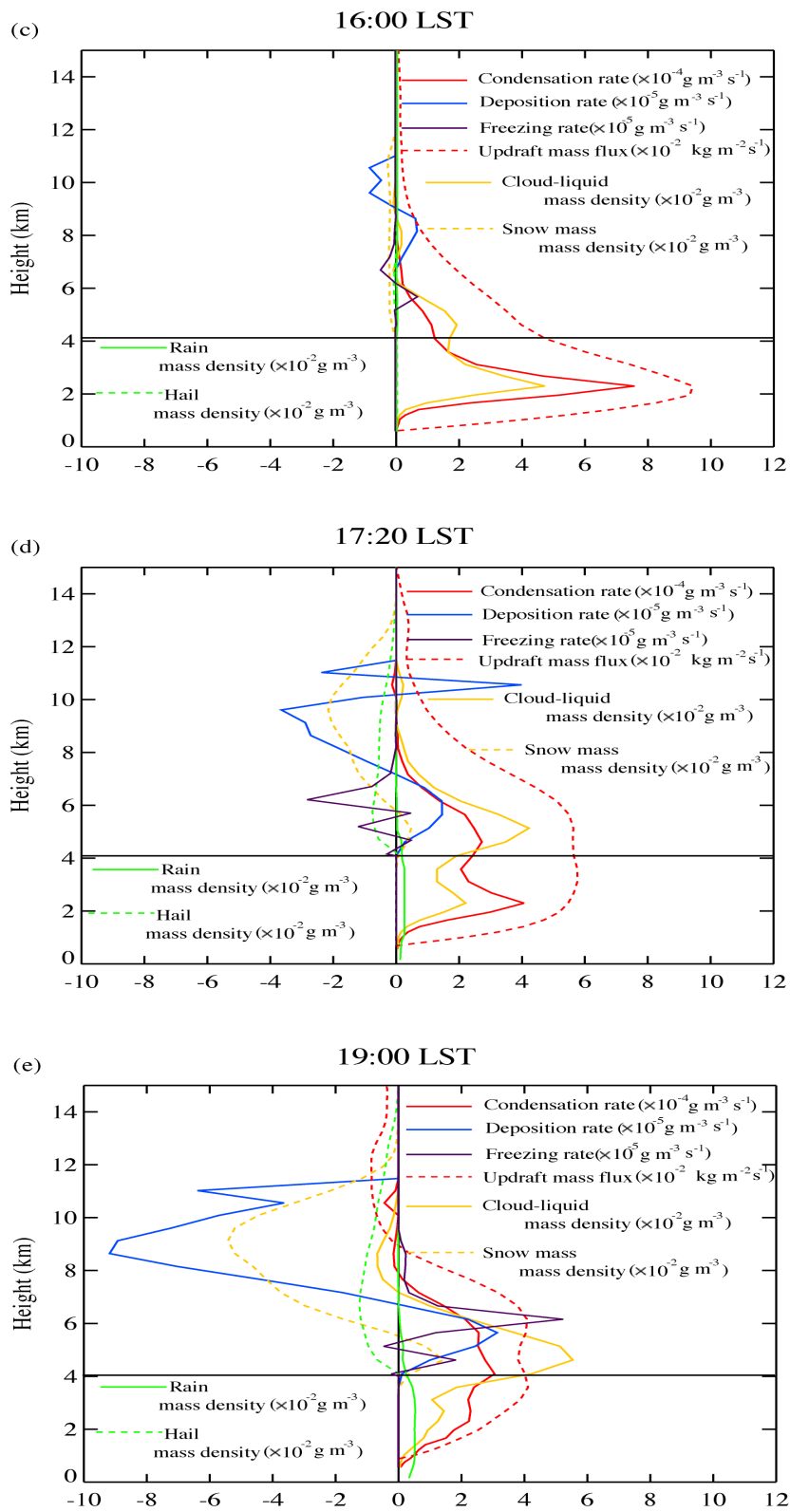
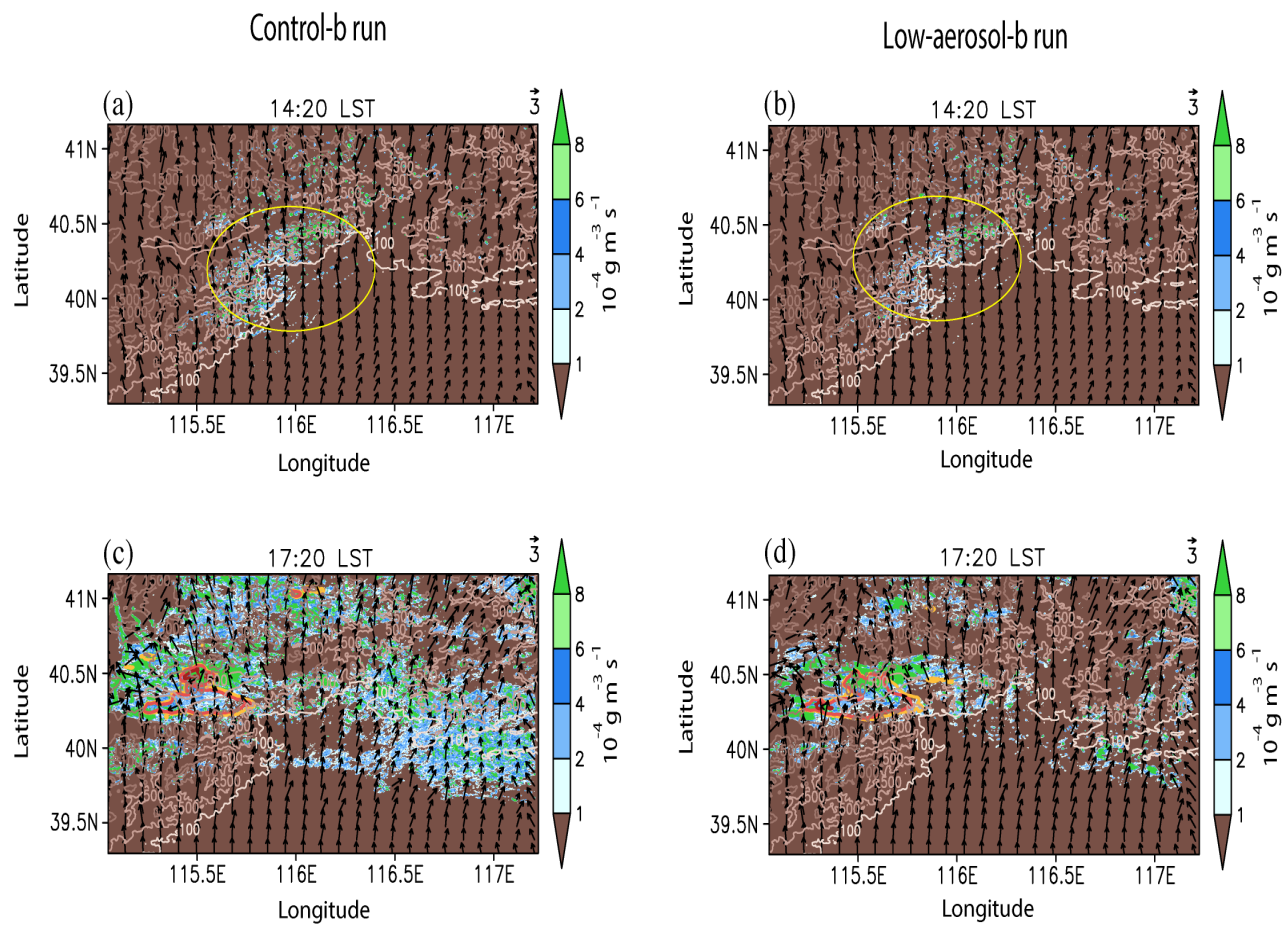


Figure 10

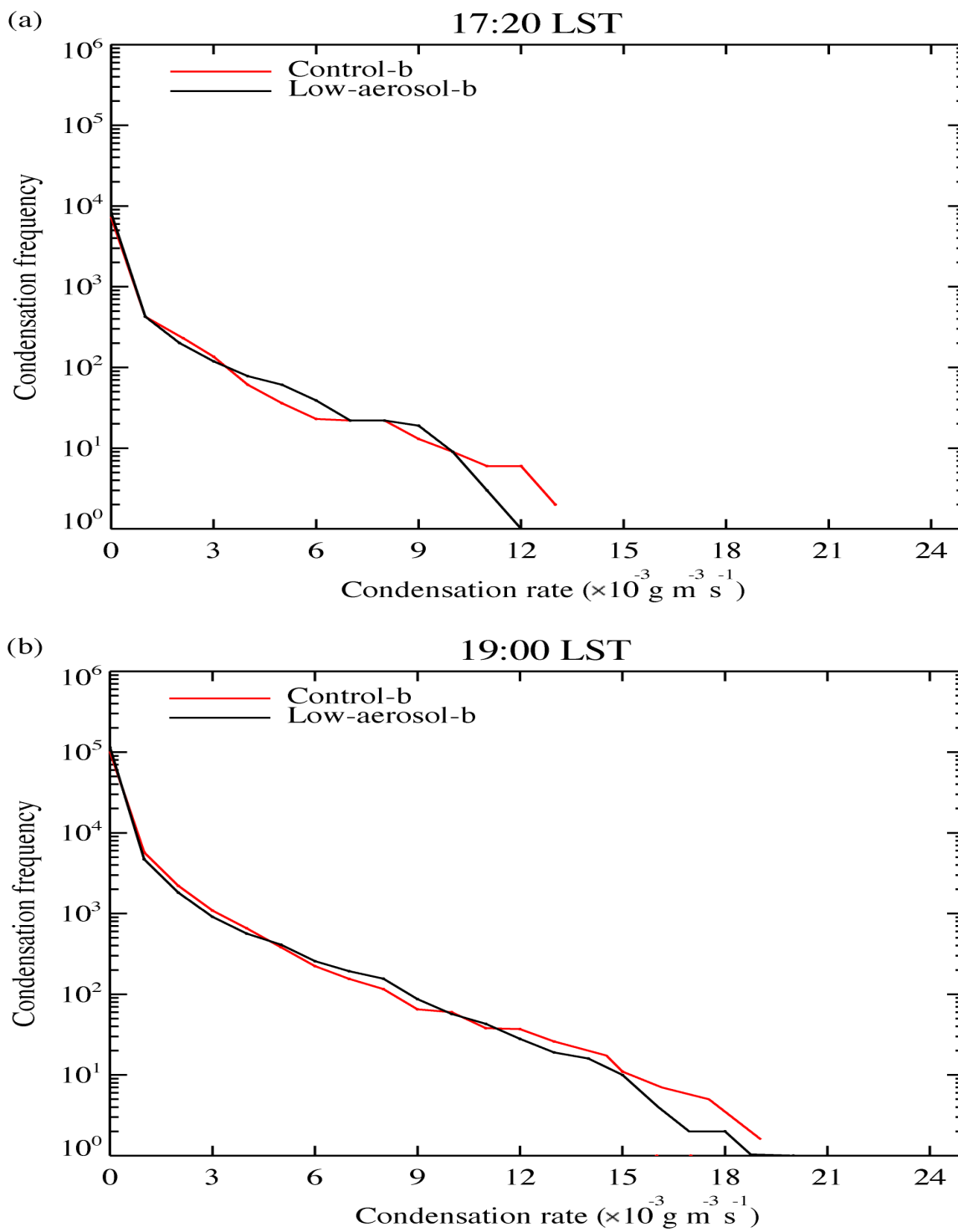
1319
1320



1321
 1322
 1323
 1324
 1325

Figure 11

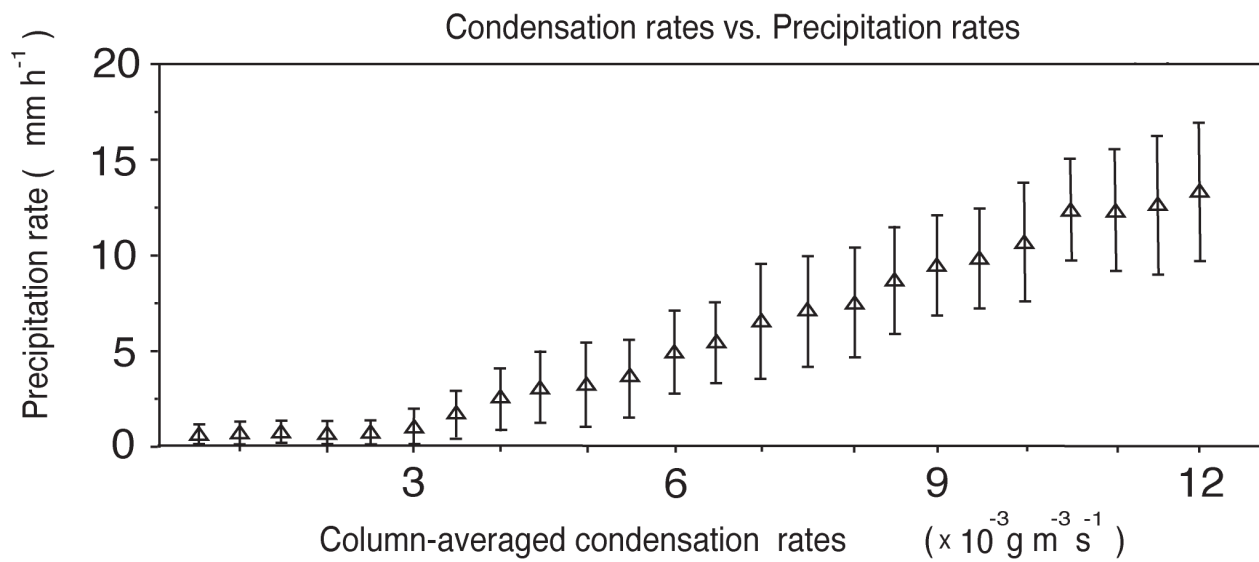
Beijing case



1326

1327

Figure 12



1328

1329

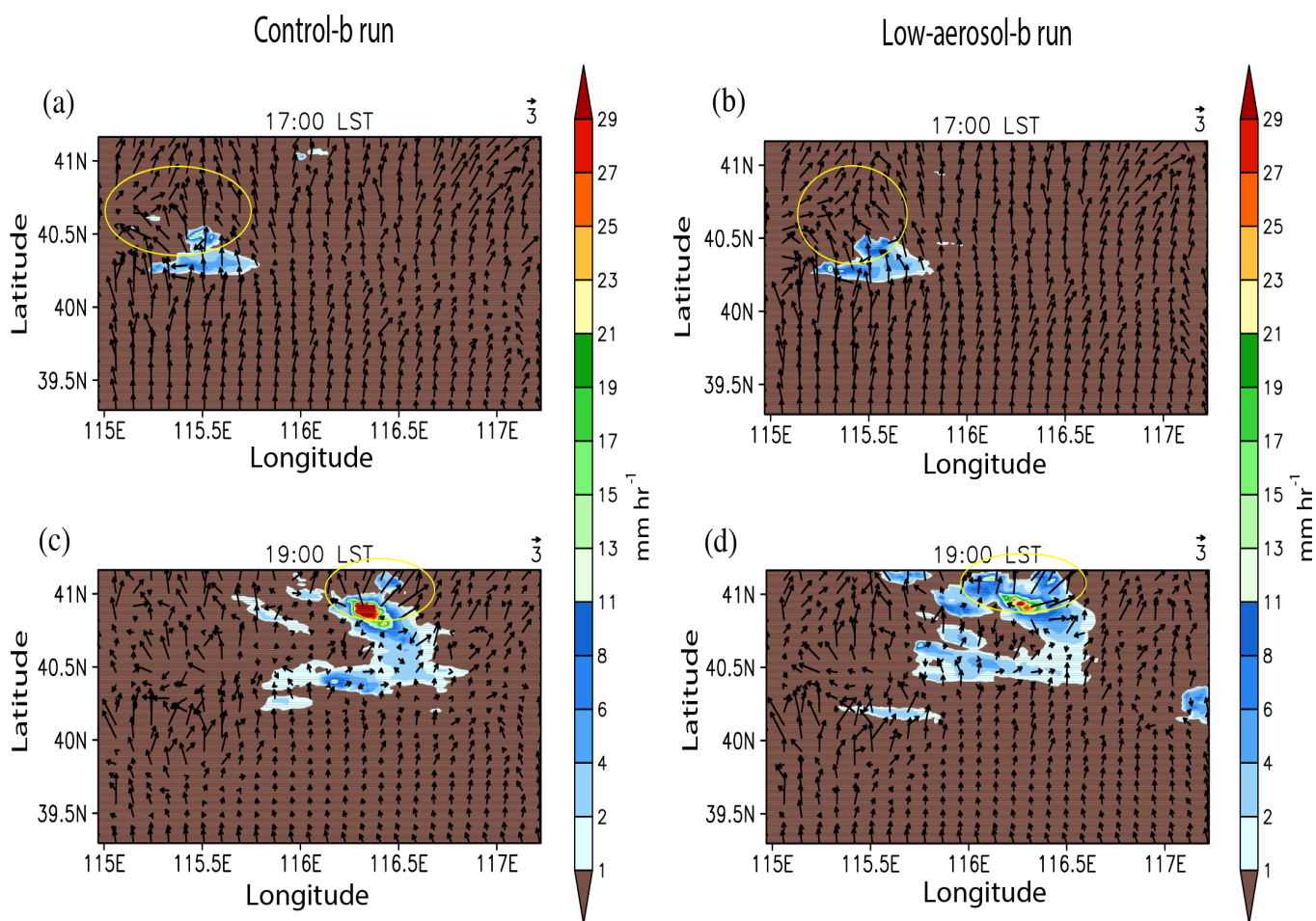
1330

1331

1332

1333

Figure 13



1334

1335

1336

1337

Figure 14